Adjustment of the Ventilated Thermocline*

WILLIAM K. DEWAR

Department of Oceanography, The Florida State University, Tallahassee, Florida

RUI X. HUANG

Department of Physical Oceanography, Woods Hole Oceanographic Institution, Woods Hole, Massachusetts

(Manuscript received 11 May 1999, in final form 1 September 2000)

ABSTRACT

The time dependence of the ventilated thermocline is examined via analytical and numerical means. The original Henderschott model is modified such that the outcrops all occur on the same geopotential surface, rather than at staggered geopotential surfaces. This model has the advantage that the ocean interior can be ventilated directly by the Sverdrup flow, rather than by western boundary processes. The propagation of disturbances governed by linearized forms of the three-layer or four-layer modified Henderschott model, nonlinear solutions of the full modified Henderschott model, and numerical solutions of the planetary geostrophic equations are considered.

Low-frequency disturbances are predicted by the linear models to move on characteristics jointly set by advection and wave dynamics. It is shown that perturbations due to wind stress anomalies project strongly onto the first mode and propagate westward similarly to the classical first baroclinic Rossby mode. They do not experience much interaction with the mean flow (the so-called non-Doppler effect). On the other hand, perturbations generated by buoyancy anomalies have strong projections onto the second or third modes, and propagate along pathways very close to the mean circulation. Their speed is somewhat slower than the current speed, however. These properties appear in the linearized and simplified nonlinear models and their occurrence in planetary geostrophic results argues the relevance of the Henderschott model. Also, these properties are consistent with results from other studies.

1. Introduction

The theory of the mean circulation of the oceans is relatively advanced in comparison to our understanding of the time-dependent circulation. As interest continues to grow in climate and climatic variability, however, questions about the variable large-scale circulation naturally arise. A major source of ocean transience is found in the time dependence of its primary forcing functions, that is, the wind and heat flux. These, in turn, are broad band and variable at decadal and interdecadal frequencies. Deser et al. (1996) have recently described the evolution of large-scale, low-frequency, (that is, decadal) buoyant anomalies in the North Pacific. Because such anomalies are of importance to climate through their effect on sea surface temperature, the study of the time-dependent large scale is strongly motivated. The objective of this paper is to analytically and numerically examine simple models of the time-dependent ventilated thermocline, with a view toward explaining the above observations.

The theory of the general circulation was advanced considerably in the early 1980s through the work of Rhines and Young (1982) and Luyten et al. (1983, LPS hereafter). These studies addressed the mechanics of subsurface flows in a stratified ocean, with the former theory describing eddy accelerations and the latter ventilation mechanics. Pedlosky and Young (1983) joined these two together within the planetary geostrophic framework of the original LPS theory and Dewar (1986) further discussed the interaction of eddies with buoyant forcing. Huang (1989), Huang and Russell (1994), and Huang and Qiu (1998) have applied the ventilated thermocline theory in continuous form to the diagnosis of the Atlantic and Pacific thermocline from surface data and thereby demonstrated the applicability of this theory to the world's oceans. Several other studies (Marshall et al. 1993; Qiu and Huang 1995) have attempted diagnoses of ventilation rates of the oceans based on sea surface wind and density observations.

A common feature of the above studies is that they

* Woods Hole Oceanographic Institution Contribution Number 9996.

Corresponding author address: Dr. William K. Dewar, Department of Oceanography, The Florida State University, Tallahassee, FL 32306-4320.
E-mail: dewar@ocean.fsu.edu

are based on an assumed steady-state structure to the ocean thermocline. It is well known that the ocean is not in equilibrium, but to the extent that significant variability in the ocean surface conditions occurs on slow temporal scales, the above studies yield valid results. The timescales required for this are not precisely known, but roughly stated are longer than the decadal timescale necessary for first-mode baroclinic planetary waves to cross the basin.

In contrast to the well-studied ''mean'' structure of the oceans, the time-dependent structure remains largely unstudied, especially within the confines of semianalytical theory. Exceptions to this are found for higher frequency, seasonal forcing (Killworth et al. 1997; Qiu et al. 1997; White et al. 1998; Dewar 1998), but these studies do not carry over to the lower-frequency case mentioned above due to some inherent simplifications they employ. Liu (1999) has discussed some aspects of ventilated thermocline variability in a multilayered model and stresses the almost orthogonal roles played by the first and second modes of the general circulation in large-scale adjustment.

More recently, Huang and Pedlosky (1999) have finessed the direct calculation of thermocline variability by computing ''before'' and ''after'' steady states differentiated by modifications to the imposed outcrops. Differencing the thermocline depth maps of these states indicated zones of transition, principally slanted to the west and southwest from the perturbed outcrops, which were presumably related to the pathways on which the surface boundary conditions worked into the interior. Wind and thermal anomalies were considered and found to elicit distinct patterns in the thermocline.

Levitus (1989) illuminated the characteristics of oceanic low-frequency ocean variability through his comparison of 5-yr averaged North Atlantic tracer fields, separated in time by 15 years. Since then, other decadal timescale ocean fluctuations have been identified. Joyce et al. (2000, manuscript submitted to *J. Climate*) have recently attempted to relate fluctuations in North Atlantic subtropical mode water to the North Atlantic Oscillation, although aside from this, connections between observed ocean thermocline variability and comparable decadal-scale atmospheric variability have been difficult to identify.

Of particular interest to this work is the paper by Deser et al. (1996), who examined thermal anomaly propagation in the subsurface Pacific. They found two rates of descent for the anomalies: a slow and persistent thermocline depth change underlying much more rapid high-frequency, seasonal events. Their analysis suggested that the ventilated thermocline provided an apparently consistent theoretical framework for the interpretation of the slower thermocline modifications, although the results were noisy. The higher-frequency events, however, moved at speeds other than those of the fluid in which they were embedded. Since they were discussing subsurface anomalies, whose genesis was presumably linked to buoyancy flux variability at the surface, this analysis seems to bear on the variability of the ventilated thermocline.

The above, particularly the latter paper, motivates our study, the primary objective of which is to examine the adjustment mechanics of the ventilated thermocline. As such, we build upon and add to the previous studies by considering the explicit time-dependent ventilated thermocline, forced by variable wind and buoyancy forcings acting in the range of decadal timescales. We propose a variant of the quasigeostrophic (QG) ventilated thermocline model developed by Henderschott (1989) and consider the temporal evolution so computed by linear and nonlinear integrations. These are strongly suggestive of the role of the first and second baroclinic modes of the general circulation in conducting anomalies about the basin. It is in the use of the Henderschott model to compute characteristics for the anomaly motions that our work differs from that of Liu (1999), who used ray tracing methods to achieve similar objectives. Comparisons of these solutions with numerical solutions of the full planetary geostrophic equations suggest that the physics of the time dependence is captured by our modified Henderschott model. We suggest the adjustment mechanics of the ventilated thermocline exhibits a strong wavelike character although the end state essentially results in anomalies downstream of the forcing anomaly. The wave input to anomaly propagation is roughly equal to the advective input, and the net propagation is like that inferred by Deser et al. (1996).

In the next section, we derive our modified Henderschott model in a three-layer system and in section 3 discuss solutions of it using linearized and full versions. These are compared in section 4 with the full planetary geostrophic solutions and the paper ends with a discussion and conclusions section. Appendix A contains a brief overview of our planetary geostrophic model and in appendix B the modified Henderschott model for a four-layer system is discussed.

2. The modified Henderschott model

The inviscid quasigeostrophic (QG) equations for a three-layer system are:

$$\frac{\partial}{\partial t}q_1 + J(\psi_1, q_1) = \frac{f_o}{H_1}w_e;$$

$$q_1 = \nabla^2\psi_1 - \frac{f_o}{H_1}h_1 + \beta y \qquad (1)$$

$$\frac{\partial}{\partial t}q_2 + J(\psi_2, q_2) = 0;$$

$$q_2 = \nabla^2\psi_2 + \frac{f_o}{H_2}(h_1 - h_2) + \beta y \qquad (2)$$

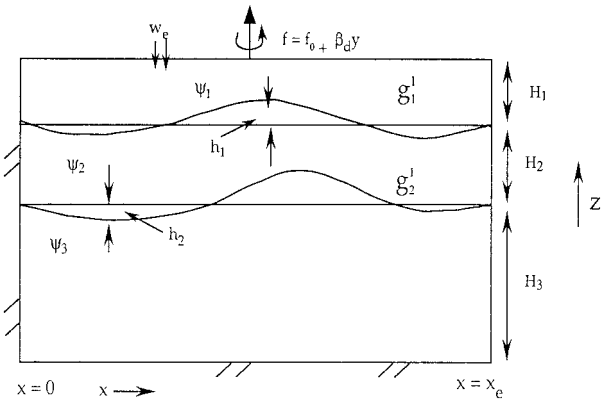

FIG. 1. Model schematic. A three-layer configuration is shown. The model is flat bottomed, forced by a variable wind, and on a β plane. Notation is standard.

$$\frac{\partial}{\partial t} q_3 + J(\psi_3, q_3) = 0;$$

$$q_3 = \nabla^2 \psi_3 + \frac{f_o}{H_3} h_2 + \beta y. \tag{3}$$

The above equations express the potential vorticity dynamics of each layer. The quantity β is the north–south gradient of the Coriolis parameter, $f = f_o + \beta y$, q_i denotes the potential vorticity of layer i, $\psi_i = p_i / f_o$ the streamfunction for layer i, p_i the layer i pressure, h_i the interface perturbation for the interface between layers i and $i + 1$ (measured positive downward), and w_e the Ekman pumping at the surface. Interface perturbations are related to streamfunctions via

$$g_i' h_i = f_o(\psi_i - \psi_{i+1}), \tag{4}$$

where g_i' is the reduced gravity parameter of interface i. A schematic zonal section of the model appears in Fig. 1.

The large-scale QG (LSQG) equations are obtained from (1)–(3) by neglecting relative vorticity, which reduces potential vorticity to contributions from the background field and vortex tube stretching. These classical equations form the basis of the original Henderschott (1989) model. The innovative part of that analysis focused on the geometry of the basin. As shown in Fig. 2a, the layers were given different meridional extents; thus, the Henderschott model in a three-layer configuration goes from a three-layer, to a two-layer, and finally to a homogeneous ocean as one moves north. The Ek-

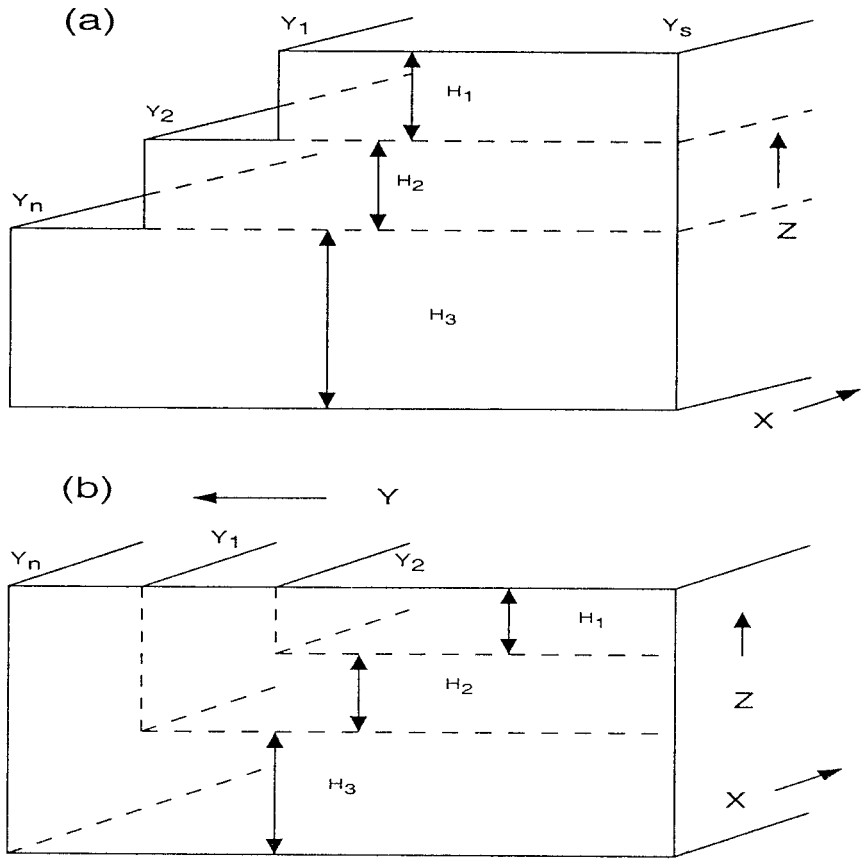

FIG. 2. The Henderschott ventilated thermocline model. (a) The classic model geometry appears in and (b) our modified geometry. The latter ventilates the surface layer directly, rather than via the western boundary. Notation is standard.

man pumping necessary to drive the flow was applied at the surface of the exposed layer and continuity of mass flux was assumed. An analog of the ventilation process thus existed in this model in that fluid north of an outcrop, directly forced by wind stress, could subduct and thereafter follow essentially a potential vorticity preserving trajectory as it moved south. There is considerable analytical advantage to the LSQG equations relative to the planetary geostrophic (PG) equations used in the original LPS theory, and this alone serves as motivation for the study of the Henderschott model.

There is in this model an analog of the LPS shadow zone, where only the surface water is in motion. This zone begins at the outcrop latitude, such as Y1 in Fig. 2, on the eastern boundary. Immediately south of this point, the surface fluid must have a southward velocity, as required by the Sverdrup constraint. It is at such a point, however, where a troublesome aspect of this model is found. A zonal flow emanating from the western boundary, and flowing east all along the outcrop, is required to feed this southward flow on the eastern boundary. Ultimately, this reflects the no mass flux condition required on the outcrop boundary. In fact, in the original Henderschott (1989) two moving layer solutions, all the surface layer flow above the ventilated flow is purely eastward. This is not a characteristic of the ventilated thermocline as formulated in the PG system. The meridional mass flux at the outcrop for the outcropped layer does vanish due to the vanishing layer thickness, but the surface geostrophic flow immediately south of the outcrop has its origins in the local Ekman pumping. Equivalently, the buoyancy in the Ekman layer has been modified such that some of the Ekman transport crosses the outcrop.

We therefore have modified the geometry of the Henderschott model to that shown in Fig. 2b in order to capture this aspect of the mass flux. Rather than exposing deeper layers to Ekman pumping at successively deeper geopotentials, we assume the surface of the fluid always occurs at the same geopotential and that the thicknesses of the layers are discontinuous at the outcrops. For this geometry, it is not obvious that the no mass flux boundary condition on the outcrop is required; different pressure boundary conditions are possible.

We will apply the boundary condition

$$\frac{f_o(\psi_i - \psi_{i+1})}{g'} = h_i = 0 \tag{5}$$

at the outcrop for layer *i*. It is possible to support this boundary condition from equations, although some fairly strong assumptions must be made. For our purposes here, we remark that (5) avoids the zonal flow required in the original model by introducing fluid into the new outcropped layer directly from the north. Boundary condition (5) may also be viewed as a mathematical convenience whose ultimate suitability depends upon how well the subsequent model predictions agree with the results of more elaborate models. The latter point will be the subject of section 4.

3. Linear and nonlinear solutions to the Henderschott model

Due to the neglect of relative vorticity in (1)–(3), the system is subject to a Sverdrup constraint. South of the outcrop, when written in terms of h_1, h_2, and P_3, this becomes

$$HP_3 + g'H_1(h_1 + 2h_2) = \frac{f_o^2}{\beta}\int_{x_e}^{x} w_e\, dx, \tag{6}$$

where it has been assumed for convenience that $H_2 = H_1$ and $g_1' = g_2' = g'$. The formula north of the outcrop is obtained from the above by suppressing h_1. The above argues that P_3 scales inversely with the total depth of the fluid, H. Thus, if the fluid is deep, P_3 may be neglected relative to the upper two layer pressures. [Note, this is not equivalent to neglecting the third layer transport in (6).] South of the outcrop, the remaining two prognostic equations for h_1 and h_2 can be written after some algebra as

$$h_{1t} - \frac{g'\beta H_1}{f_o^2}(h_1 + h_2)_x + \frac{g'}{f_o}J(h_2, h_1) = -w_e \tag{7}$$

$$h_{2t} - \frac{\beta g' H_1}{f_o^2}(h_1 + 2h_2)_x = -w_e, \tag{8}$$

where suppression of h_1 in (8) yields the appropriate h_2 equation north of the outcrop.

First we discuss the form the above model takes when linearized about a mean circulation. Specifically, we assume the wind stress and buoyancy fluxes (equivalent to outcrop specification) are known and largely steady. These generate a mean flow. Weak perturbations to these forcing fields are assumed that, in turn, generate small pressure fluctuations that must propagate in the presence of β and the mean circulation.

Writing the unknowns in terms of mean and perturbation contributions and defining $g'H_1/f_o^2 = R_d^2$ yields the mean field equations

$$h_{1o} + 2h_{2o} = \phi = \frac{1}{\beta R_d^2} w_e(x - x_e) \quad \text{and} \tag{9}$$

$$J\left(h_{2o}, \beta R_d^2 y + \frac{g'}{f_o}\phi\right) = 0 \tag{10}$$

south of the outcrop, where it has been assumed for convenience that the Ekman pumping is a function of latitude only. Suppressing h_{1o} in (9) yields the governing equation north of the outcrop.

These equations define the mean field and their solution is discussed in many places. Examples of the mean pressure fields so generated appear in Fig. 3, where the Ekman pumping field

$$w_e = \mu_o y/L, \qquad -L/2 < y < 0 \tag{11}$$

$$w_e = \mu_o(y + L)/L, \qquad -L < y < -L/2 \tag{12}$$

has been used. The parameter values used in Fig. 3 are $\beta = 2 \times 10^{-11}$ m s^{-1}, $L = 2000$ km, $f_o = 10^{-4}$ s^{-1}, $H_1 = 500$ m, $\mu_o = 1 \times 10^{-6}$ m s^{-1}, and $g' = 0.02$ m s^{-2}. The formula for the pressure field north of the outcrop is

$$p_{2o} = \frac{f_o^2}{2\beta H_1}\frac{\mu_o y}{L}(x - x_e). \tag{13}$$

South of the outcrop,

$$p_{1o} = \frac{f_o^2}{\beta H_1}\frac{\mu_o y}{L}(x - x_e) \tag{14}$$

$$p_{2o} = 0 \tag{15}$$

for $(x_e - x) > \beta^2 g' H_1^2 L(y - y_o)/(f_o^3 \mu_o y)$, where y_o denotes the outcrop position and

$$p_{1o} = \frac{f_o^2 \mu_o y(x - x_e)}{2\beta H_1 L} - \frac{\beta g' H_1(y - y_o)}{2 f_o} \tag{16}$$

$$p_{2o} = \frac{f_o^2 \mu_o y(x - x_e)}{2H_1 \beta L} + \frac{\beta g' H_1(y - y_o)}{2 f_o} \tag{17}$$

elsewhere south of the outcrop. It has been assumed that y_o occurs north of $y = -L/2$ and the solution for the northern half basin only has been written. Note the apparent southward mass flux out of the outcrop in layer 1 (Fig. 3a).

We now develop the linearized equations for the perturbation interface thickness. After some algebra, and denoting the perturbation to Ekman pumping by w_e' these become

$$h_{2t} - \frac{2\beta g' H_1}{f_o^2} h_{2x} = -w_e' \tag{18}$$

north of the outcrop and

$$h_{1t} - \frac{g' H_1 \beta}{f_o^2}(h_1 + h_2)_x + \frac{g'}{f_o}[J(h_{2o}, h_1) + J(h_2, h_{1o})] = -w_e' \tag{19}$$

$$h_{2t} - \beta\frac{g' H_1}{f_o^2}(h_1 + 2h_2)_x = -w_e' \tag{20}$$

south of the outcrop.

It is useful to rewrite (19) and (20) using the normal modes associated with the resting state (i.e., in the absence of a mean flow). Defining separation constants $(\alpha_+, \alpha_-) = [1 + \sqrt{(5)}]/2, [1 - \sqrt{(5)}]/2)$, the first and second resting state baroclinic modes can be written as

$$h_+ = h_1 + \alpha_+ h_2 \quad \text{and} \tag{21}$$

$$h_- = h_1 + \alpha_- h_2. \tag{22}$$

In terms of h_+, h_-, (19) and (20) become

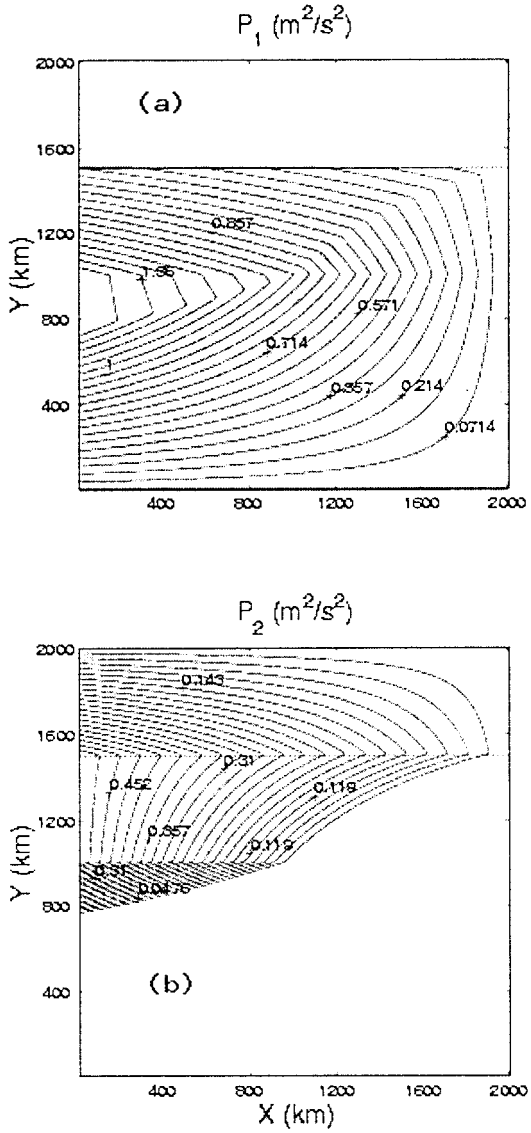

FIG. 3. Mean fields for the linear modified Henderschott model. The pressure field for (a) layer 1 and (b) layer 2.

$$h_{+t} + J(\chi_1, h_+) = J(H_+, h_-) - (1 + \alpha_+)w_e' \tag{23}$$

$$h_{-t} + J(\chi_2, h_-) = -J(H_-, h_+) - (1 + \alpha_-)w_e', \tag{24}$$

where

$$H_+ = \frac{g'}{f_0(\alpha_- - \alpha_+)}(h_{1o} + \alpha_+ h_{2o}) \tag{25}$$

$$H_- = \frac{g'}{f_0(\alpha_- - \alpha_+)}(h_{1o} + \alpha_- h_{2o}) \tag{26}$$

$$\chi_1 = \beta_+ y + H_- \tag{27}$$

$$\chi_2 = \beta_- y - H_+ \tag{28}$$

$\beta_+ = \beta R_d^2(1 + \alpha_+)$, and $\beta_- = \beta R_d^2(1 + \alpha_-)$. These equations highlight the role played by the mean flow in

both steering and manufacturing modal anomalies. The quantities χ_1 and χ_2 act as characteristics in our model and will appear frequently in the upcoming analysis.

Since the zonal velocity along these characteristics is dominated by the β effect,

$$\frac{|u_{\chi_1}|}{|u_{\chi_2}|} \approx \frac{1 + \alpha_+}{1 + \alpha_-} \approx \frac{2.618}{0.382} \gg 1. \tag{29}$$

Similarly, the meridional velocity along these characteristics has a ratio

$$\frac{|v_{\chi_1}|}{|v_{\chi_2}|} = \frac{|(h_{1o} + \alpha_+ h_{2o})_x|}{|(h_{1o} + \alpha_- h_{2o})_x|} \approx \frac{|-2 + \alpha_+|}{|-2 + \alpha_-|} \approx \frac{0.382}{2.618} \ll 1. \tag{30}$$

In the above, for estimation purposes, we have assumed h_{1o} scales like $2h_{2o}$. Therefore, zonal propagation of signals along χ_1 is much faster than χ_2, but meridional propagation of signals along χ_1 is much slower than χ_2.

The above system consists of two coupled first-order, nonconstant coefficient, linear equations. However, in spite of their apparent simplicity, *there is no known general technique for their exact solution.* The value of this analysis lies in the illustration of the mean flow–perturbation interactions. The first baroclinic mode, h_+, which largely measures the in-phase movements of the thermocline, experiences characteristics involving β and the second mode of the mean circulation, $h_{o-} = h_{1o} + \alpha_- h_{2o}$. The characteristics affecting the second baroclinic mode, h_-, which measures out-of-phase thermocline movements, involves β and the first mode of the general circulation, $h_{1o} + \alpha_+ h_{2o}$. This might have been anticipated given the recent analyses of near-annual-frequency baroclinic planetary waves in the general circulation (Killworth et al. 1997; Dewar 1998), which found a similar influence on the first mode perturbations.

The new parts are the right-hand sides that couple the modes together. Here, one sees the first perturbation mode is forced by the second mode, operating in the presence of the first general circulation mode, and the second perturbation mode is forced by the first mode operating through the second general circulation mode. In the near-annual forcing case mentioned above, a spatial averaging of (23) is useful because second mode waves are short compared to first mode waves, which in turn are short compared to the basin scale. The result of the averaging is an uncoupled single first mode equation, whose analytical solution can be obtained. Here, we are interested in lower-frequency forcing anomalies, in which case the above scale arguments are not valid and the full forms of (23) and (24) must be considered. In view of their general analytical insolubility, we resort to numerical solutions. However, we first show maps of the first and second mode characteristics, χ_1, and χ_2 in Fig. 4, where the mean fields in Fig. 3 have been used. Note that over parts of the domain near the outcrop, these characteristics are largely orthogonal, with χ_1 generating zonal motion and χ_2 meridional. These features of the characteristics are insensitive to the specific mean fields used here and will be key to understanding the upcoming numerical solutions.

Finally, the steady solution of the perturbation equations can be obtained analytically. This is done by suppressing the time derivatives in (19) and (20), from which it is seen that the solution of (20) is immediate. Eliminating h_1 in favor of h_2 in (19) yields one equation in one unknown whose solution depends upon boundary data and the perturbations to forcing. These solutions are intrinsically related to those generated by Huang and Pedlosky (1999). We will model buoyancy flux perturbations as movements in the outcrop locations. Wind perturbations are modeled using the fluctuation Ekman pumping, w'_e. We have considered cases of each individually and jointly.

It is straightforward to solve the fully time-dependent modified Henderschott model in (7)–(8) numerically. Below, we present several such solutions. We have used standard numerical procedures; that is, an Arakawa fourth-order-accurate enstrophy and energy conserving formulation was used to compute the Jacobians, leapfrog time stepping with infrequent averaging of adjacent time levels was employed, and the equations were augmented by a weak diffusion of both h_1 and h_2 for stability reasons. The latter were evaluated at the lagged time step. Horizontal resolution was 10 km in both dimensions, and time steps of 2 h were used.

a. Buoyancy perturbations

1) STEADY ANOMALIES

We consider localized, but large scale, buoyancy perturbations, in the same manner as Huang and Pedlosky (1999). Two types of experiments are conducted. In the first, we implement a perturbation to the outcrop, and then hold it fixed. In the second, we vary the perturbation sinusoidally in time using a range of frequencies. Our model parameters are such that a first mode wave will cross the basin in about 2.5 years. We therefore consider forcing frequencies of durations equal to or greater than this.

Parallel to Huang and Pedlosky (1999), the perturbation solution as $t \to \infty$ can be found by subtracting the old steady solution from the new, perturbed but steady solution; thus

$$\delta h_2 \approx -\frac{\beta g' H_1}{2 f_o} \delta y > 0, \tag{31}$$

where $\delta y = y_{\text{new}} - y_0 < 0$. Since there is no wind stress anomaly, from (8) one obtains

$$\delta h_1 = -2\delta h_2 < 0. \tag{32}$$

At $t = 0^+$, a step-function perturbation in the outcrop

line sets the perturbations in δh_1 and δh_2 along the perturbed outcrop line, so

$$\delta h_+^0 = \delta h_1 + \alpha_+ \delta h_2 = -0.382 \delta h_2 \quad (33)$$

$$\delta h_-^0 = \delta h_1 + \alpha_- \delta h_2 = -2.618 \delta h_2. \quad (34)$$

Thus, $|\delta h_-^0| \gg |\delta h_+^0|$; that is, the perturbations induced by the cooling/heating have a strong projection onto the second mode and a weak projection onto the first mode. Further, the slight projection on the first mode will be relatively confined meridionally and move zonally rather rapidly to the western boundary. The primary response of the system will thus be in the second mode and the χ_2 characteristics will move buoyancy anomalies into the interior. Since the second mode waves move southward much faster than the first mode waves, $h_+ = 0$ along the leading edge of the second mode wave response, and the source term on the right-hand side of (24) is negligible near this wave front. Thus, perturbations initially imposed on the outcrop line are conserved and propagated with the wave front. In a model without mixing, these perturbations would propagate southwestward conserving their amplitude; however, the finite mixing in our numerical model gradually reduces the amplitude of the anomaly downstream. (By varying the mixing in our model, we have confirmed that mixing controls the perturbation amplitude in the downstream direction.) The strength of the first mode excitation by the second mode downstream of the imposed forcing anomaly will be small, for the reason that first mode amplitude will be accumulated along the χ_1 characteristics, which cut more or less at right angles to the primary second mode disturbance. These in turn are confined zonally, so the small amplitude second mode forces the first mode over a ''short'' distance. The result is a second-order response in the first mode. We stress that these predictions for the behavior of the system come from the structure of the linearized equations. We now compare those predictions with solutions obtained by integrating the full nonlinear set (7)–(8).

A sequence of basin plan views is given in Fig. 5 of an experiment in which the outcrop position was changed suddenly and thereafter held fixed. The model was begun from a state of rest and run under unperturbed conditions for a period of roughly 40 years. The final state was assumed to represent the mean field of the system. The outcrop location was changed and the model was subsequently run for another 15 years. First and second interface depths were archived at intervals of a quarter-year. The mean fields were subtracted from the archived fields to yield plots of the first and second interface perturbations. These were combined according to (21) and (22) to generate fields of first and second mode amplitudes.

First mode amplitude plots appear in Figs. 5a–d and the second mode in Figs. 5e–h. The time intervals corresponding to the plots are 1, 3, 5, and 10 years after the stationary perturbation is applied to the outcrop. The initial outcrop location is denoted in all figures by the solid zonal line. The nonzonal dashed line denotes the location of the perturbed outcrop.

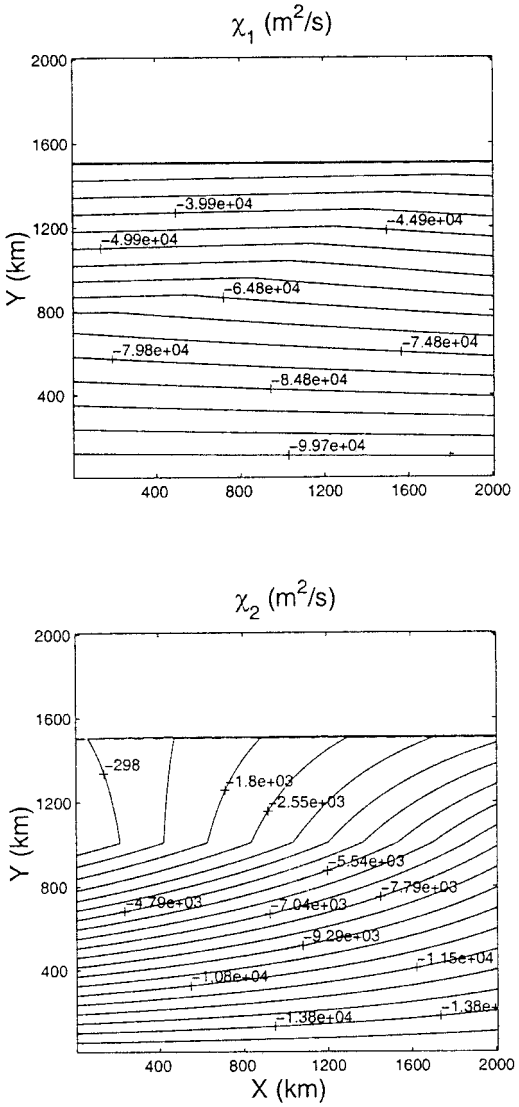

FIG. 4. The χ_1 and χ_2 characteristics for the modified Henderschott model.

There is a region of small-scale activity in all plots located in the southwestern corner of the domain. This is a zone where the meridional gradient of potential vorticity changes with depth, thus meeting the necessary condition for baroclinic instability. The length scale of the variability is controlled by the thickness diffusion coefficient, as several experiments (not shown here) have demonstrated. As our analysis is incapable of describing such dynamics, we focus instead on the remainder of the circulation where broad scales characteristic of the general circulation dominate.

The basic interpretation of these plots is in agreement with the behavior anticipated from the linearized equations. Namely, the short-term initial first mode adjust-

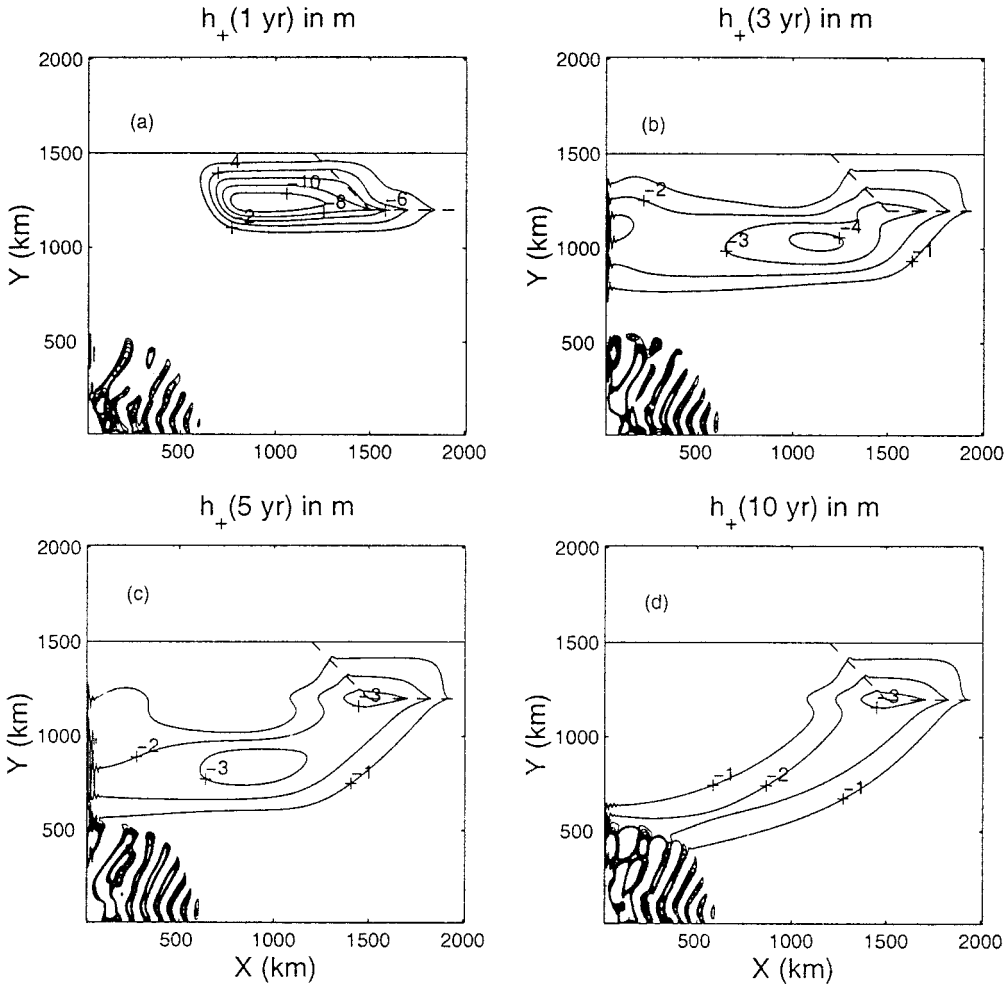

FIG. 4. (*Continued*)

ment is confined meridionally and moves zonally to the western edge of the basin (Figs. 5a,b). The second mode amplitude thereafter dominates and the anomaly moves largely on a trajectory set by the χ_2 characteristics (Figs. 5e–h). As the latter propagates, a weaker tendency for first mode amplitude to reach westward from the second mode anomaly is noted (Figs. 5b–d). This weak first mode excitation tracks the movement of the second mode anomaly. Eventually, the transient part of the response disappears into the western boundary.

The wake of the initial outcrop disturbance appears both in the first and second modes; thus, it is seen that both modes participate in the establishment of the eventual steady solution. The steady solution this system approaches is essentially like that predicted by Huang and Pedlosky (1999). What we demonstrate here is the rather curious manner by which this steady state is obtained. Several points are worth noting. First, the anomaly pattern moves along a pathway that is substantially different that the associated fluid velocities. In effect, this reflects that a significant part of the adjustment to a forcing anomaly is wavelike, rather than advective. Second, although the details of the modal transients are very different, and the excitation of the two occurs with very different amplitudes, the resulting steady state involves both at leading order. At least in this case, the steady first mode response is generated secondarily by the second mode; the direct first mode response to the anomaly is effectively completely flushed from the system.

Although the projection of our solution onto these two sets of characteristics clearly show the wave activity west of the subduction pathway, these waves may be difficult to diagnose from climate data for the following reasons. First, waves along the χ_1 characteristics are overpowered by waves along the χ_2 characteristics. We have the inverse relations

$$h_1 = \frac{\alpha_- h_+ - \alpha_+ h_-}{\alpha_- - \alpha_+} \approx \frac{-0.618 h_+ + 1.618 h_-}{2.236} \tag{35}$$

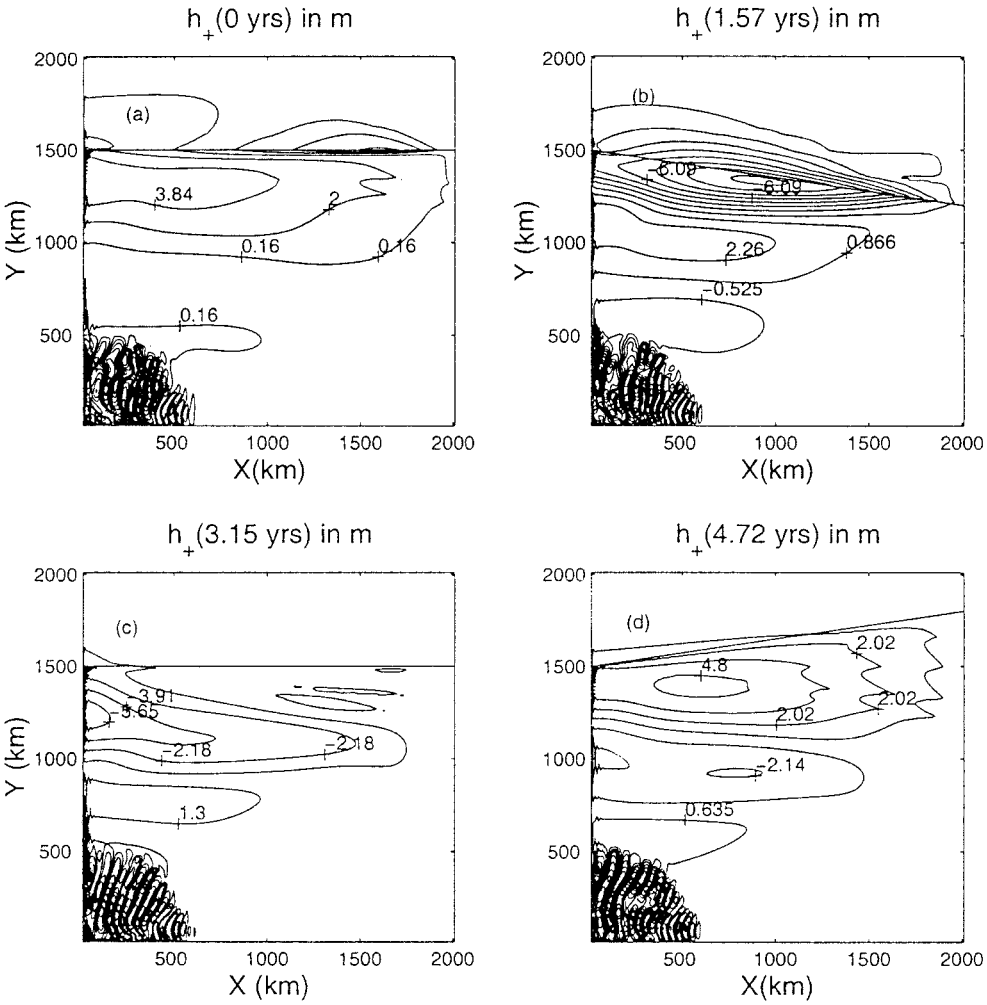

FIG. 5. The adjustment of the nonlinear modified Henderschott model to a maintained outcrop perturbation. The spatial structures of the initial and perturbed outcrops appear in all figures and are denoted by the solid and dashed lines. Amplitude at (a) 1 yr, (b) 3 yr, (c) 5 yr, and (d) 10 yr for the first mode and (e) 1 yr, (f) 3 yr, (g) 5 yr, and (h) 10 yr for the second mode is contoured.

$$h_1 - h_2 = \frac{(1 - \alpha_-)h_+ + (1 - \alpha_+)h_-}{\alpha_- - \alpha_+}$$

$$\approx \frac{1.618h_+ + 0.618h_-}{2.236} \qquad (36)$$

(note that we include a formula for $h_1 - h_2$ rather than for h_2, as the former represents thermocline thickness anomalies and is of interest to climate variability). Thus, the upper interface displacement is primarily controlled by h_-, while the h_+ contribution is smaller by roughly a factor of 3. On the other hand, the contribution to the thermocline thickness anomaly from the h_+ waves is about 2.5 times larger than that of the second baroclinic mode. Thus, wave activity west of the subduction pathway, where the second mode will be weak, may be easier to identify from the relative interfacial displacements of the deeper interfaces. This will appear in the results from the multilayer PG model.

2) OSCILLATING FORCING ANOMALIES

An example of the thermocline response to a low-frequency variable buoyancy anomaly is shown in Figs. 6a–h. Here, the frequency is 1 cycle $(6.3\ \text{yr})^{-1}$ and modal amplitudes at quarter phases of the forcing are shown. These results were generated by running the modified Henderschott model for 63 years with the variable forcing. Results from only the last 6.3 yr are shown. The thicknesses from the last oscillation cycle were averaged to produce measures of the mean fields. These were removed from the archived data and the residuals were combined via (21) and (22) to yield maps of h_+ and h_-. The nature of the forcing is a simple tilting of the otherwise zonal outcrop. The maximum peak to trough amplitude of the oscillation (occurring on the eastern side of the basin) is 600 km , while on the western basin side the front is fixed. The location of the front appears in all the plots and is denoted by the bold straight line.

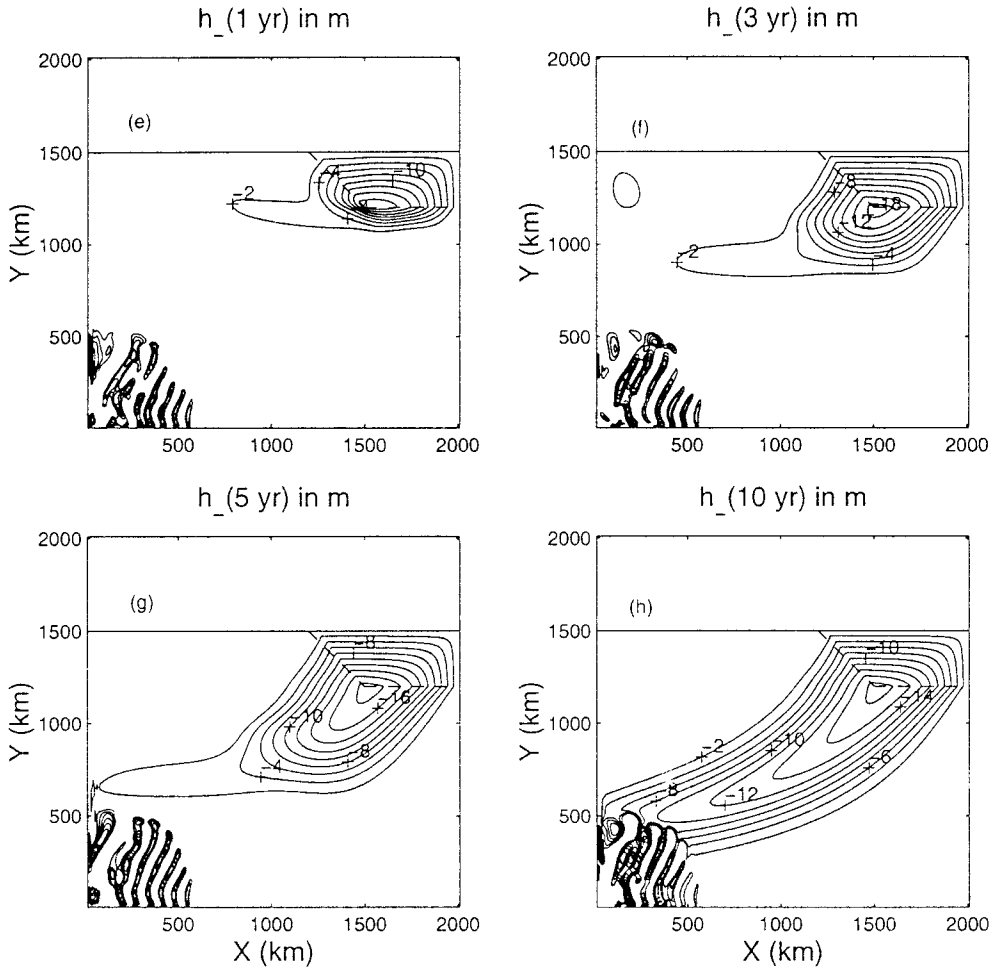

FIG. 5. (*Continued*)

The first mode amplitude is seen to be comparable here to that of the second mode. This is a characteristic of time-dependent solutions that differs with our previous steady-state response estimates. Aside from this, the response is in essential agreement with the behavior expected from the linearized equations as discussed previously. Now, the direct first and second mode responses are continually generated, and the primary signal propagates in cones defined by the χ_1 and χ_2 fields. The largest first mode response occurs in the zonal band defined by the range of the outcrop oscillation. In contrast, the second mode propagates effectively into the circulation interior, moving along the χ_2 characteristics. There is now a wavelength along the χ_2 tracks of the second mode, as opposed to the impulsively applied and maintained case in Fig. 5. This occurs because the phase of the forcing changes and opposite signs of the modal anomaly are generated. Note that weak first mode variability is seen west of the second mode track, again in keeping with qualitative behavior suggested by the linearized equations.

In a sense, these results most convincingly demonstrate the value of the linearized analysis. The amplitude maps in Fig. 6 are complex [those of the interface perturbations themselves (not shown here) are in fact more so]. Without the guidance of the linearized analysis, it would be difficult to interpret the plots.

b. Wind perturbations

We show in Fig. 7 results of an experiment in which the outcrop was held fixed and the Ekman pumping was varied. The spatial structure of w_e' was the same as the mean w_e. Ekman pumping was modulated sinusoidally at a frequency of 1 cycle (12. 6 yr)$^{-1}$ and the amplitude of the pumping perturbation was set at 1×10^{-7} m s^{-1}, that is, at 10% of the value of the mean Ekman pumping. The time required by a simple first mode baroclinic wave to cross the basin is roughly 2.5 yr, so this forcing is seen to be very slow. Plan views of the basin at 0, 3.15, 6.3, and 9.45 yr after the point of maximum downwelling are shown.

In contrast to the thermal forcing anomaly, the wind stress anomaly has a strong projection onto the first

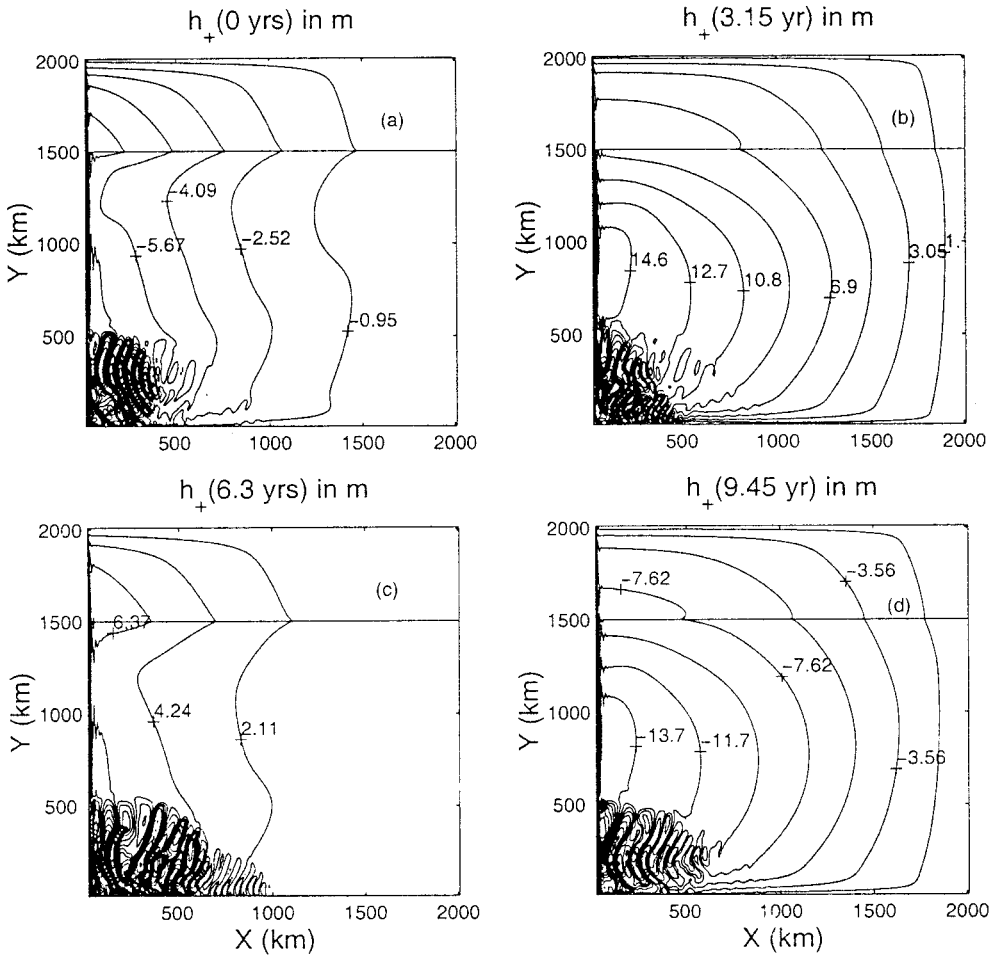

FIG. 6. Adjustment of the modified Henderschott model to a variable perturbation of the outcrop. The frequency of the perturbation is 6.3 yr and output at quarter phases of the forcing are shown, that is, (a) 0 yr, (b) 1.57 yr, (c) 3.15 yr, and (d) 4.72 yr for mode 1, and (e) 0 yr, (f) 1.57 yr, (g) 3.15 yr, and (h) 4.72 yr for mode 2. The outcrop location appears in all figures as the bold straight.

mode and a weak projection onto the second mode. This is consistent with the right-hand sides of (23) and (24), because the forcing ratio

$$\frac{1 + \alpha_+}{1 - \alpha_-} \approx \frac{2.618}{0.382} = 6.85 \gg 1.$$

As discussed above, first mode anomaly propagation is largely zonal. The second mode, in contrast, is strongly refracted by the mean circulation and is seen to experience a strong anticyclonic perturbation from a purely zonal displacement. Variations of the propagation of both modes about the linear nondispersive speed are due to interactions with the mean flow, as described in Killworth et al. (1997) and Dewar (1998). The qualitative resemblance of the phase propagation to the χ_1 and χ_2 characteristics is clear.

Experiments with an impulsively applied wind stress perturbation are not shown here because the results can be anticipated from the preceding figures. The modal responses largely reflect the χ_1 and χ_2 characteristics.

4. Comparisons with planetary geostrophic experiments

The modified Henderschott model discussed above is valuable for the analytical convenience it brings to this problem. This, in turn, is realized at the cost of the explicit appearance of outcrops as are permitted in the planetary geostrophic equations. The validity of the modified Henderschott model thus rests upon the illustration of predicted behaviors in integrations of the PG equations. These are discussed in this section.

We used the PG model originally developed by Huang and Bryan (1987). This is a layered model based on geostrophy and the full continuity equation. A Kraus-Turner mixed layer 50 m deep is included on top. Buoyancy is introduced into the interior via the redistribution mechanism discussed in Huang (1989). Explicit western boundary layer dynamics are included, albeit in a relatively viscous form. It is nonetheless important to point out this distinction, for this model can recycle anomalies

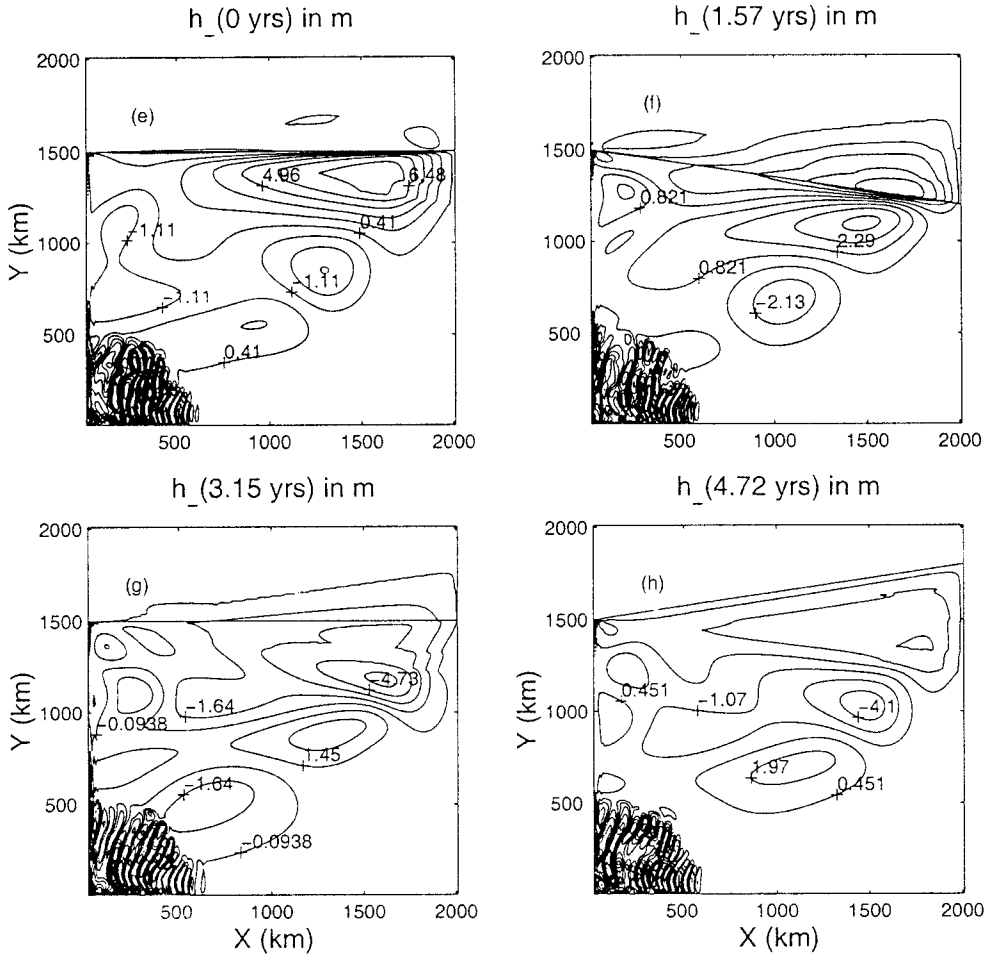

FIG. 6. (*Continued*)

back into the interior via western boundary advection, as will be seen. Momentum exchange between layers occurs via interfacial drag coefficients and, finally, the outcrop location is computed as part of the circulation. This contrasts with the a priori outcrop specification as appears here and in the ventilated thermocline model of Huang and Pedlosky (1999). A more thorough discussion of our PG model is included in appendix A. In all, our PG model is very complete; at coarse resolution, it is essentially a primitive equation general circulation model. It is also a very complex model compared to the modified Henderschott model discussed in sections 2 and 3.

The emphasis in this paper on ventilation mechanics prompts us here to discuss explicitly the changes induced in the interior by surface heating and cooling anomalies. These cause, via anomalous diapycnal mass fluxes, interior thickness anomalies. For example, for a cooling anomaly, movements of the middle and lower interfaces, that is, $\Delta(h_1 + h_2)$ and $\Delta(h_1 + h_2 + h_3)$ are both positive, while the upper interface shoals (Δh_1 is negative). This is consistent with the net heat loss caused by the anomalous cooling.

Our PG model includes four interior layers and a mixed layer. Of the interior layers, the deepest is assumed to be very thick, leaving three active layers. Before presenting the anomalous solutions, it is therefore useful to examine the structure of the modified Henderschott model with four layers. (Recall that for the time-dependent problem, even layers that are not directly ventilated in the subtropical gyre will support nontrivial flows.) The details can be found in appendix B. Most importantly, we derive the linearized characteristics there, which prove helpful in understanding the PG model behavior. The pertinent parameters are $L_x = 6000$ km, $L_y = 3000$ km, the second layer outcrops along $y = 2000$ km, $\beta = 2.0 \times 10^{-11}$ (m s)$^{-1}$, and $f_o = 10^{-4}$ s^{-1}. The Ekman pumping is $w_e = w_0 \sin(\pi y/L_y)$, where $w_0 = 10^{-6}$ m s^{-1}. As seen in Fig. 8, the χ_1 characteristics are primarily zonal, while the χ_2 and χ_3 characteristics appear to follow the streamlines in the ventilated thermocline layers. In fact, the difference between the χ_2

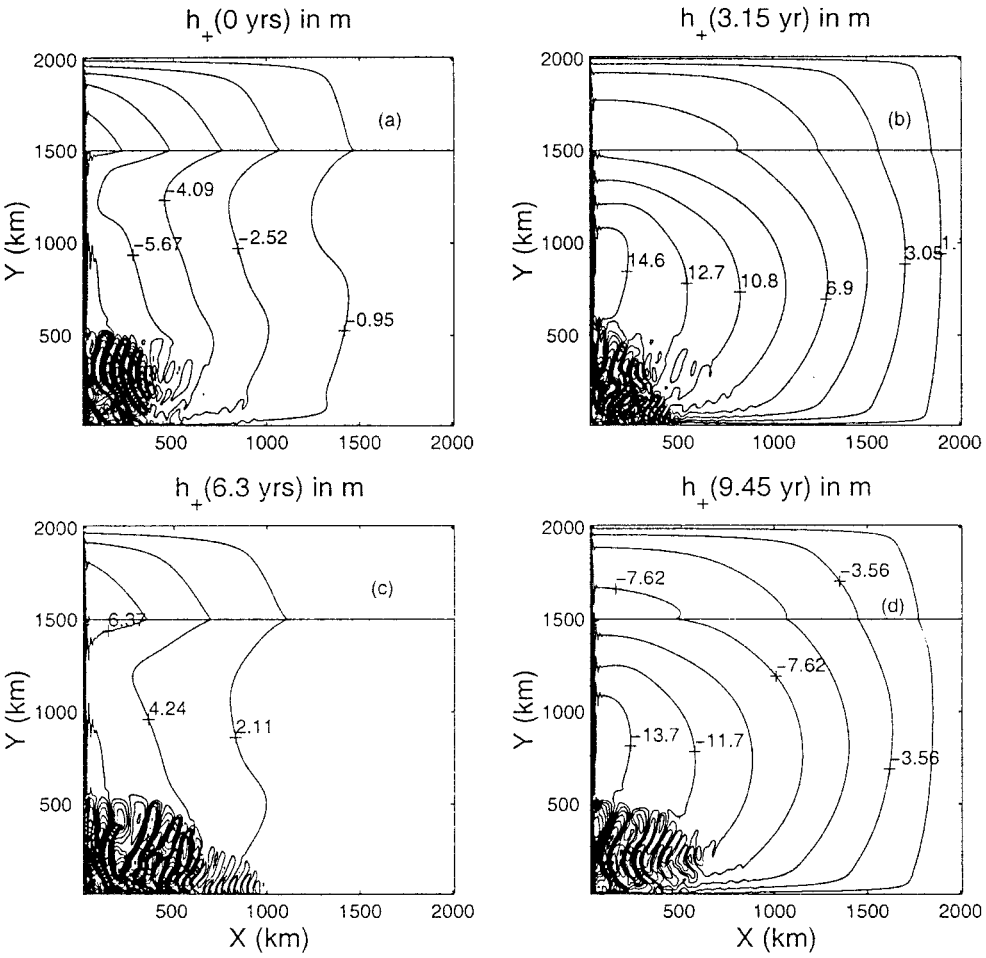

FIG. 7. Adjustment to a variable Ekman pumping perturbation. The amplitude of the global Ekman pumping field was oscillated with a period of 12.6 yr. First and second mode amplitudes at quarter phases of the forcing (i.e., 0, 3.15, 6.3, and 9.45 yr) from the point of maximum downwelling are shown.

characteristics and the streamlines in the second layer is rather small (see Fig. 9). (Note that both Figs. 8 and 9 are based on formulas for the classical ventilated region west of the shadow zone, because this is the focus of the present study.)

An important point is that the signal speed along the second and third characteristics is slightly smaller than that of the horizontal advection speed in both layers 2 and 3 (see Fig. 10 where velocity profiles through the middle of the basin are shown). Meridional velocity in layer 1 is quite different from that in layers 2 and 3 because the upper layer is directly exposed to Ekman pumping. It is also interesting that the characteristic speed along χ_3 is slightly higher than that along χ_2 but, nevertheless, smaller than the current speed. This implies that buoyant anomalies tend to propagate along subduction pathways at speeds somewhat slower than advection.

Returning to our PG model, our basic states were spun up by specifying a linearly varying surface density (temperature) field and relaxing the mixed layer density (temperature) toward it. A fixed wind stress pattern of classical two-gyre basin structure was also imposed. The model was then integrated for 100 years under these fixed conditions. Viscosities and diffusivities were sufficient to generate (essentially) steady circulations. Some mild time dependence appeared to be unavoidable in much of our PG work. This consisted of rapid thermocline variability confined to the southern quarter of the domain. These disturbances were trapped to the southern boundary and were judged to not be of crucial importance to the phenomena under investigation. They are possibly related to the baroclinic instability seen in the modified Henderschott model. In Fig. 11, the top layer thickness of the steady solution of the model is shown. The outcrop line occurs near the extreme contour line (labeled 0.5). (The next layer down outcrops far into the subpolar gyre and is not shown here.) We next initiated variability in the forcing fields. Near the edge of the outcrop line, we altered the imposed surface reference density field within the dashed circle in Fig. 11.

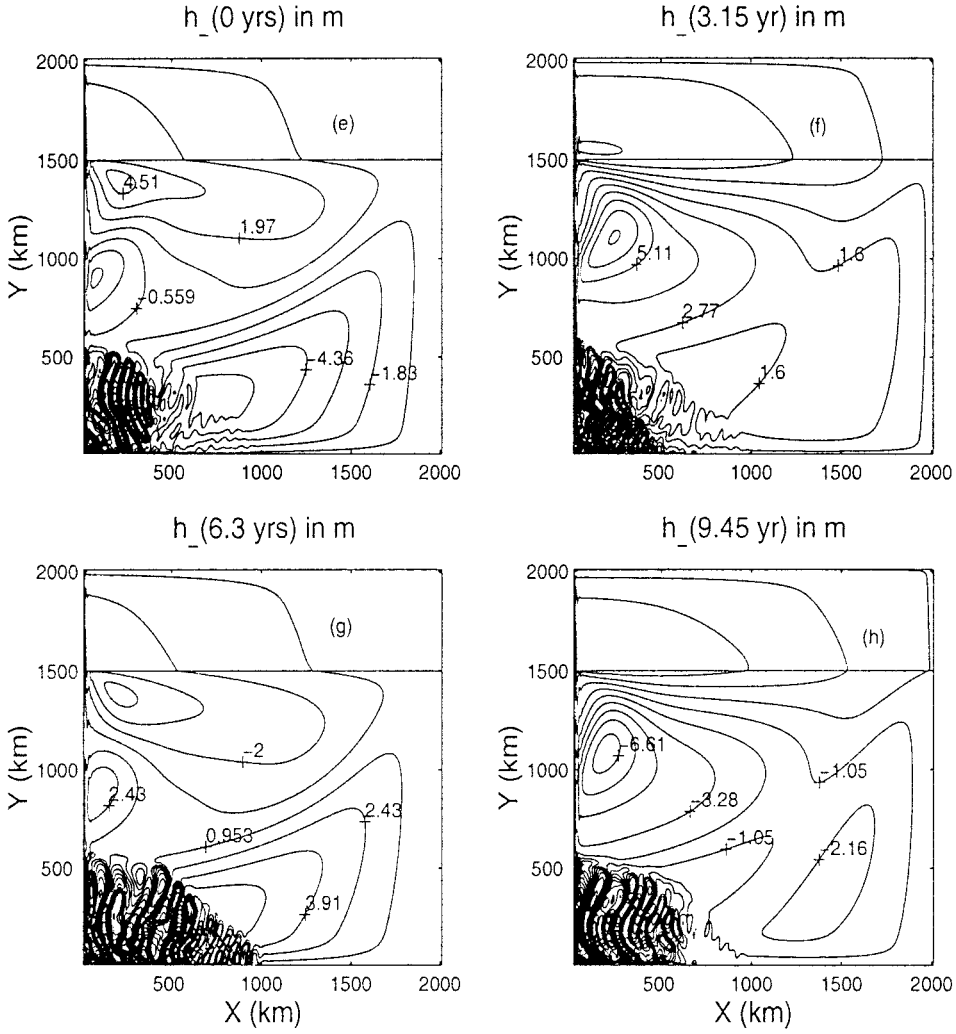

FIG. 7. (*Continued*)

The perturbation was in the form of a Gaussian profile with a maximum density change of 0.3 σ.

The top layer thicknesses after the anomaly was initiated were archived and subsequently differenced with the fields in Fig. 11 to yield maps of the interface perturbations (see Fig. 12). (Note that in this section our results are presented in terms of interfacial displacement rather than modal amplitudes. This is because this is the format commonly used in oceanic climate data analysis.) These results are from a ''high'' resolution case (120 $\times$ 120, with grid resolution 50 $\times$ 50 km). This finer grid allowed us to reduce the horizontal momentum mixing coefficient from 10^4 m^2 s^{-1} to 2 $\times$ 10^3 m^2 s^{-1}. The perturbations due to surface cooling propagate largely along subduction pathways, and within about 25 years the solution reached a quasi-steady state.

We also note that the cold tongue weakens downstream as compared with the idealized solution computed earlier here and by Huang and Pedlosky (1999). This is apparently related to the diffusion in the present model, while the result by Huang and Pedlosky (1999) is nondiffusive. Vertical mixing exerts considerable control on the nature of the ventilation anomaly. Experiments using diapycnal mixing coefficients μ from 1.3 to 0.65 cm^2 s^{-1} showed the control of the downstream extent of the cold, ventilated thermocline tongue by mixing.

By looking at the upper layer anomaly alone, one may mistakenly infer that perturbations propagate along the χ_2 characteristics alone. However, the perturbations in the second interfacial depth show that there is also significant wave input to anomaly propagation (see Fig. 13). This figure shows that the perturbations appear in the form of a second baroclinic mode, that is, shoaling of the upper interface and deepening of the second interface and the third interface. In terms of temperature, the anomaly is cold near surface, and warm deeper. This is similar to the structure computed by Huang and Pedlosky (1999). By following the negative contours (dashed lines) in Fig. 13, one can see the interaction

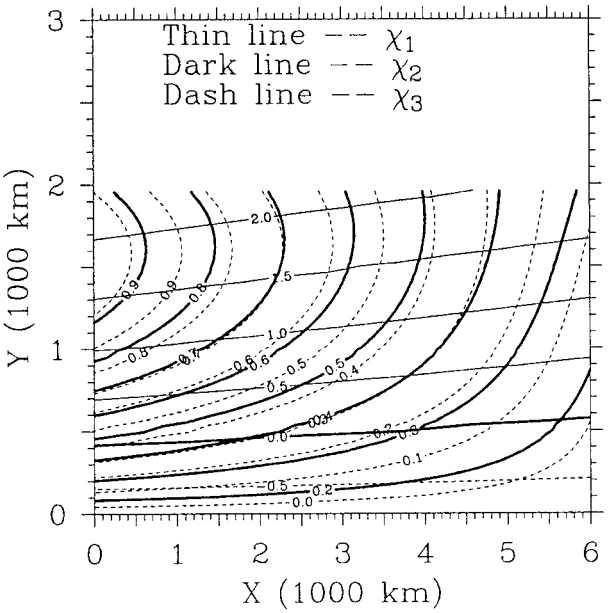

FIG. 8. Characteristics for a four-layer generalized Henderschott model.

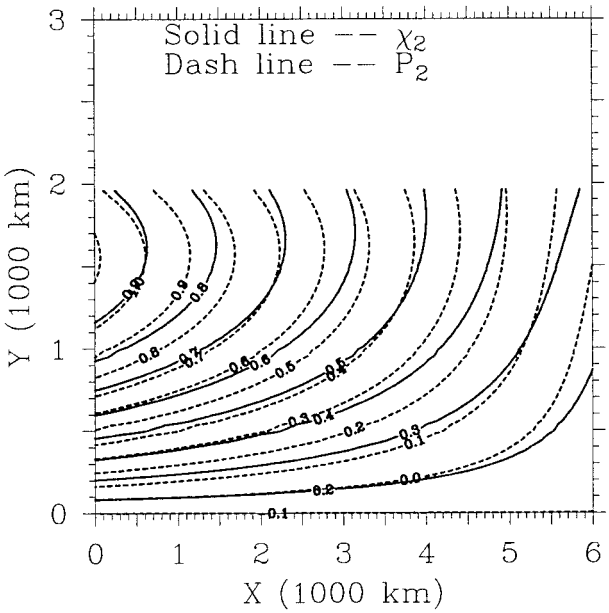

FIG. 9. Characteristics χ_2 and the streamline in the second layer.

between the first, second, and third characteristics in the fashion suggested by the Henderschott model. As the interfacial perturbations move into the interior, there are weak anomalies appearing as negative contours generated west of the main perturbation. These secondary perturbations are carried to the western boundary and recycle through the western boundary current. As time progresses, these secondary waves also move southward, following the primary perturbation. This scenario is analogous to that predicted by the QG modified Henderschott model and supports the applicability of those dynamics to the PG case.

Wind-forcing anomalies

Finally, we present an example of perturbations due to a wind stress anomaly. The model is restarted using a steady state like the solution shown in Fig. 11 and subjected to an anomalous wind stress curl within the dashed circle. This, of course, generates an Ekman pumping anomaly, the form of which is Gaussian with anomalous amplitude -0.3×10^{-6} m s^{-1}.

Our results (see Figs. 14 and 15) show activity not inconsistent with expectations based on both the modified Henderschott model and the theoretical analysis in Huang and Pedlosky (1999), although the PG model is in ways more complicated in response than either the-

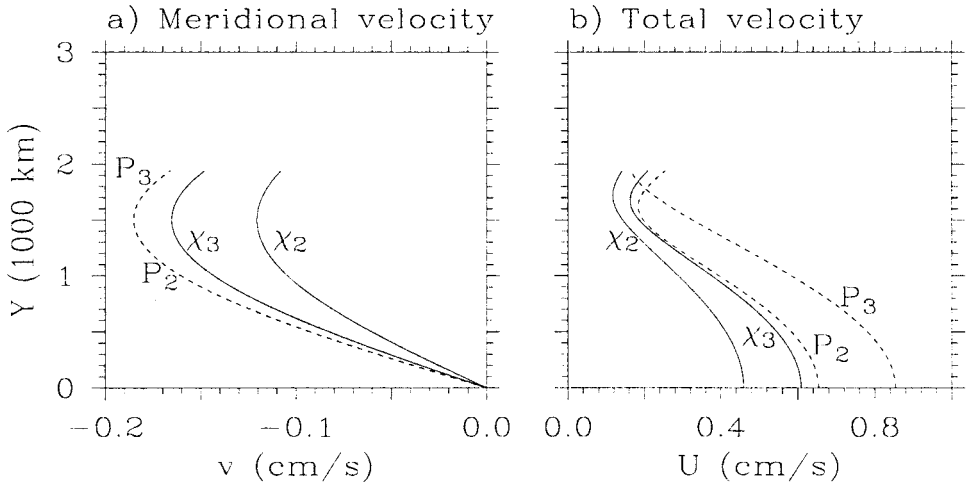

FIG. 10. Velocity in the second and third layers and along the χ_2 and χ_3 characteristics: (a) meridional velocity and (b) total velocity.

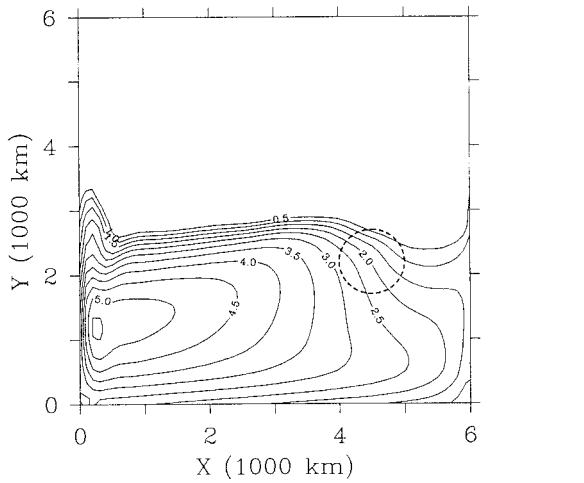

FIG. 11. The thickness of the first ventilated layer of the steady solution. The dashed circle indicates the location of the surface cooling.

ory. For example, it was assumed that Ekman pumping anomalies do not affect the outcrop line in the theories, whereas in our numerical model the outcrop line does migrate as a result of the perturbation in the wind stress. Other aspects of the model response near the outcrop latitudes also lie outside the realm of any of the above theories. Nevertheless, our numerical solution does exhibit the main features in the ocean interior discussed above, and also by Huang and Pedlosky (1999). For example, the theory predicts that if the outcrop line is nonzonal, there will be perturbations that appear in the second baroclinic mode, propagating southwest of the Ekman pumping anomaly. Indeed, there is a shoaling of the upper interface and a deepening of the second interface southwest of the Ekman pumping anomaly (centered at $x = 4500$ km). In addition, both the upper and second interfaces move downward west of the Ekman pumping anomaly, consistent with the first baroclinic mode behavior predicted from the theories. Similar to the case with cooling, the solution reaches quasi-equilibrium about 20 years after the initial perturbations. In addition, the numerical solution has a more complicated structure, especially near the western boundary where waves reflection and other dynamic components contribute to the features different from the simple theoretical prediction.

5. Discussion

We have investigated the time evolution of the thermocline subjected to anomalous forcing. It has been useful to study a variant of the so-called Henderschott model, which is a model rooted in quasigeostrophic dynamics, but includes ventilation mechanics. Our modification consists of introducing layers of variable leading order thickness inside the domain as models of outcrops. When linearized about a mean state, this model predicts the transient behavior of the ventilated thermocline will be dominated by sets of characteristics reflecting the modal decomposition of the mean state. As such, anomalies will move at rates dependent upon which thermocline mode they preferentially excite, and the characteristics upon which that mode moves. Secondary excitation of all modes is also expected, although the propagation characteristics of those modes can be greatly different from the primary mode. The resultant steady state emerging from maintained perturbations to the forcing fields ultimately involves all modes, so the secondarily excited modes are of importance.

Climate variability excited by surface forcing anomalies in the real ocean does not separate cleanly into simple vertical modes. Perhaps better descriptors are the so-called dynamical thermocline modes (DTMs), recently proposed by Huang and Pedlosky (2000), whose vertical structure varies with the variable background thermocline structure. At any given horizontal location, the local form of the DTMs resemble classical QG baroclinic modes (e.g., the second DTM has both upward and downward deflections, like the classical second baroclinic mode). Because DTMs are not entirely separable, perturbations cannot be ''projected'' exactly onto these modes.

Using a three-layer model, we have shown in this paper that perturbations due to an Ekman pumping anomaly are similar to a first DTM, while perturbations due to thermal anomalies are like a second DTM. Although ours is a few-layer model, we feel this is a relatively robust result. Huang (2000) has conducted related experiments using a continuously stratified, steady model and found second DTM structures excited by buoyant forcing anomalies. The response also involves higher DTMs, but experiments show that perturbations are preferentially confined to low modes.

The time-dependent behaviors in this paper are representative of how such modes participate in thermocline adjustment. Perturbations in forms similar to second or third modes propagate along wave characteristics that are very close to the streamlines of the ventilated thermocline, with a speed that is slightly slower than the local horizontal advection. Furthermore, secondary waves are generated west of these primary waves. They move rapidly to the west and may not be seen in the quasi-steady state. It may therefore be difficult to recognize such perturbations in climatological data.

These theoretical findings provide a context for the analysis of Deser et al. (1996), who have argued that buoyant anomalies exhibit some similarities to the ventilated thermocline theory in their subsurface propagation. Our analysis illustrates a role for wave properties of the subsurface ocean in anomaly motion. It is surprising the extent to which the dispersal of heat, largely a material oceanic property, can be affected by wave mechanics.

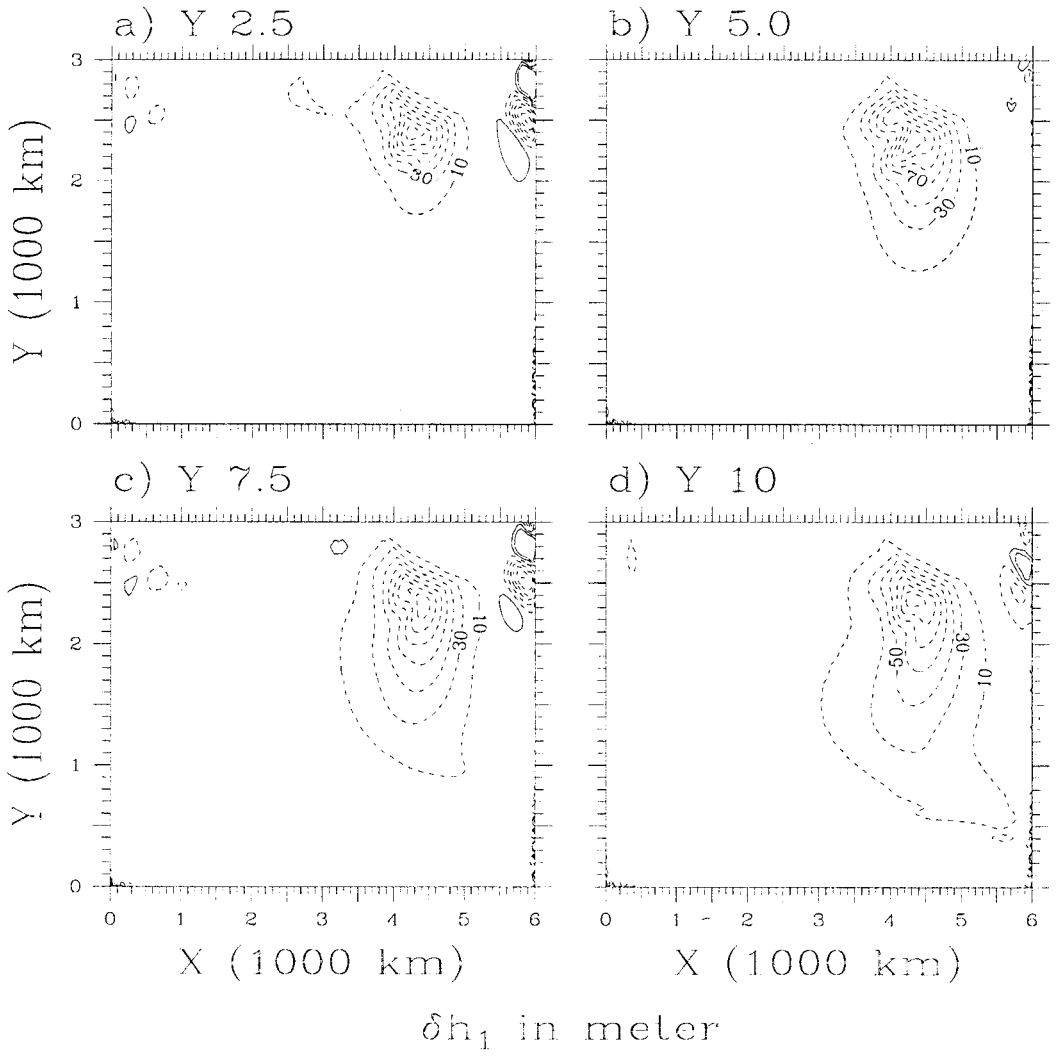

FIG. 12. Thickness anomaly in the first ventilated layer after surface cooling, obtained from a high-resolution model (grid size is 50 km).

Acknowledgments. WKD is supported through NSF Grant OCE-9617728 and NASA Grant NAG5-4813. RXH is supported through NSF Grant OCE-9616950. This work was begun while RXH was a visitor to The Florida State University. Sheila Derby aided in manuscript and figure preparation and Jane Jimeian assisted with many computational issues.

APPENDIX A

The Planetary Geostrophic Model

The model used in this study is a hybrid, multilayer model by Huang and Bryan (1987). The model is formulated on a midlatitude β plane, with a mixed layer of constant thickness on the top, and four isopycnal layers below. Since our primary goal is to explore climate variability on decadal timescales, we neglect the time-dependent terms and the inertial terms in the momentum equations; that is,

$$-fh_1v_1 + k_1(u_1 - u_2) = -h_1P_{1x}/\rho_0 + A_m\nabla(h_1\nabla u_1) + \tau/\rho_0 \quad \text{(A1)}$$

$$fh_1u_1 + k_1(v_1 - v_2) = -h_1P_{1y}/\rho_0 + A_m\nabla(h_1\nabla v_1) \quad \text{(A2)}$$

$$-fh_iv_i + k_{i-1}(u_i - u_{i-1}) + k_i(u_i - u_{i+1}) = -h_iP_{ix}/\rho_i + A_m\nabla(h_i\nabla u_i), \qquad i = 2, 3, 4, 5 \quad \text{(A3)}$$

$$fh_iu_i + k_{i-1}(v_i - v_{i-1}) + k_i(v_i - v_{i+1}) = -h_iP_{iy}/\rho_i + A_m\nabla(h_i\nabla v_i) \quad \text{(A4)}$$

$$h_{it} + (u_ih_i)_x + (v_ih_i) = e^i_{i-1} + e^i_{i+1}, \quad \text{(A5)}$$

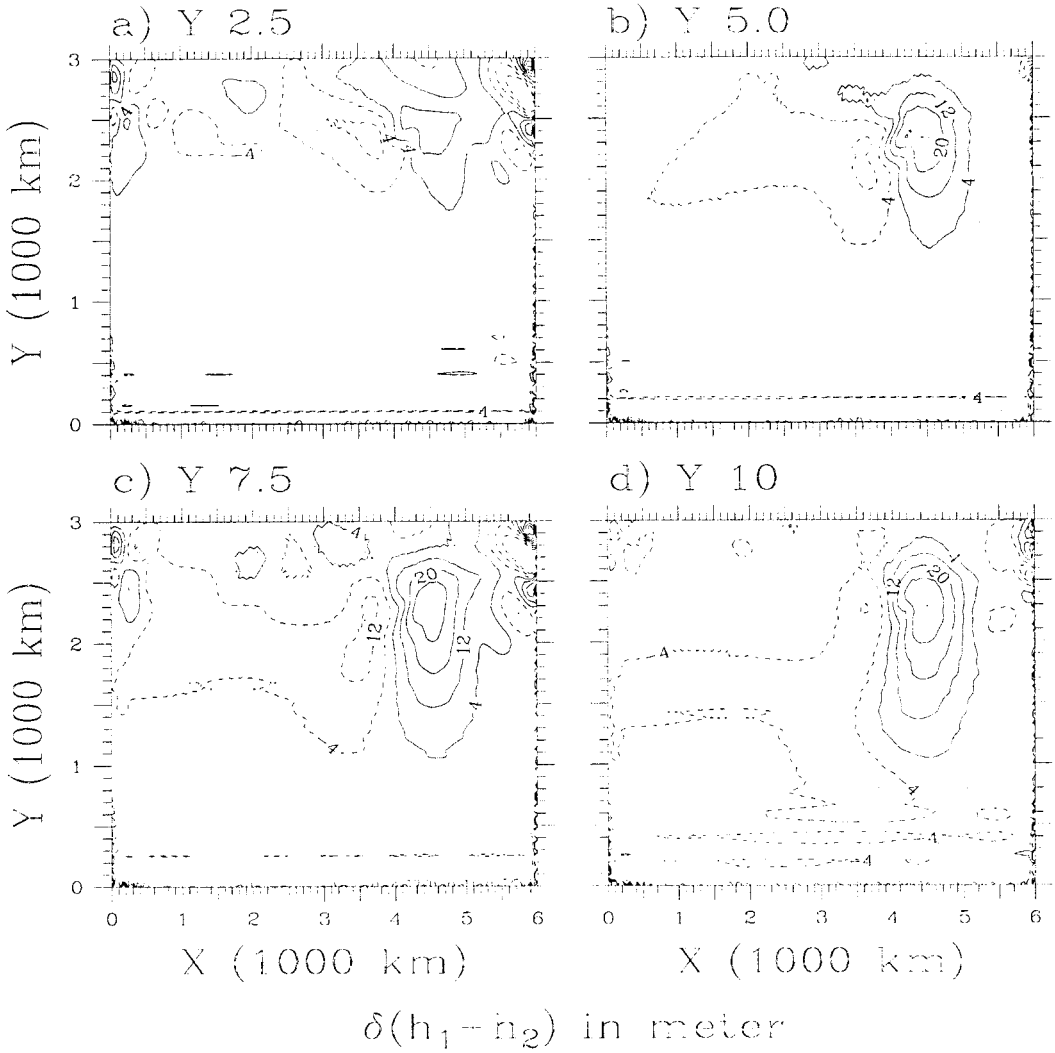

FIG. 13. Depth anomaly of the interface between the second and third layers after surface cooling, obtained from a high-resolution model (grid size is 50 km).

where h_i now denotes total layer thickness and e_i^j net entrainment from layer j into layer i; k_i represents interfacial friction coefficients.

The horizontal pressure gradient terms are calculated using the hydrostatic approximation

$$\nabla P_4 = \nabla P_5 + g_4'\nabla(h_1 + h_2 + h_3 + h_4) \quad \text{(A6)}$$

$$\nabla P_3 = \nabla P_4 + g_3'\nabla(h_1 + h_2 + h_3) \quad \text{(A7)}$$

$$\nabla P_2 = \nabla P_3 + g_2'\nabla(h_1 + h_2) \quad \text{(A8)}$$

$$\nabla P_1 = \nabla P_2 + g_1'\nabla h_1 - 0.5gh_1\nabla\rho_1, \quad \text{(A9)}$$

where $g_i' = g(\rho_{i+1}) - \rho_i)/\rho_0$ is the reduced gravity for the ith layer. In the case of steady circulation, one frequently assumes that the lowest layer is very deep, and that the pressure gradient there can be neglected. However, for a time-dependent problem the lowest layer transport must be accounted for, even if the lowest layer is very thick. As is shown in this study, neglecting the contribution from the lowest layer to transport and to pressure gradients introduces substantial errors. A pressure correction term should be included in models of the time-dependent behavior of the thermocline. In the ocean interior, friction is negligible and for the long timescales we are interested in, the time required for the barotropic adjustment is short. Thus to a good approximation, the vertically integrated volume flux satisfies the Sverdrup relation

$$\beta \sum_{i=1}^{5} h_i v_i = -\frac{\tau_y}{\rho_0}. \quad \text{(A10)}$$

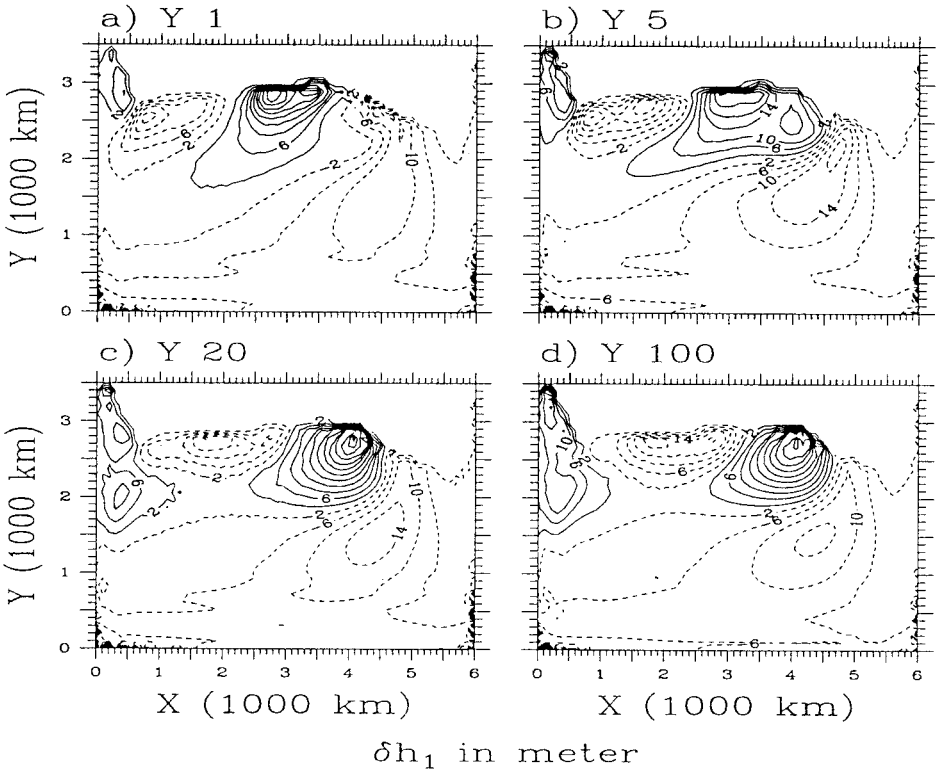

FIG. 14. Thickness anomaly in the first ventilated layer after the enhancement of Ekman pumping, obtained from a 60 × 60 model (grid size is 100 km).

We can thus diagnose the lowest layer pressure, P_5, according to

$$P_5 = \Phi - \frac{P}{H}, \tag{A11}$$

where

$$\Phi = \frac{f^2}{\beta H}\int_{x_e}^{x} k\cdot\nabla\times\frac{\boldsymbol{\tau}}{f}\,dx + \frac{0.5g}{H}\int_{x_e}^{x} h_1^2\rho_{1x}\,dx + \frac{P_e}{H}. \tag{A12}$$

The quantity P_e is the value of P along the eastern boundary and P is given by

$$P = 0.5g'_{1234}h_1^2 + g'_{234}h_1h_2 + g'_{34}h_1h_3 + g'_4h_1h_4 \tag{A13}$$

$$+0.5g'_{1234}h_2^2 + g'_{34}h_2h_3 + g'_4h_2h_4 + 0.5g'_{34}h_3^2 + g'_4h_3h_4 + 0.5g'_4h_4^2, \tag{A14}$$

where $g'_{1234} = g'_1 + g'_2 + g'_3 + g'_4$ and so on. The details of the buoyancy conservation for the mixed layer, the continuity equations for the layers below the mixed layer, and finite-difference scheme, including the convective adjustment, can be found in Huang and Bryan (1987).

APPENDIX B

A Four-Layer Modified Henderschott Model

We now formulate the modified Henderschott model with four layers, including a very deep fourth layer. South of the outcrop line, $y < y_2$, all four layers are in motion:

$$\frac{f_0(p_2-p_1)_t}{g'H_1} + \frac{1}{f_0}J\left[p_1, \frac{f_0(p_2-p_1)}{g'H_1} + \beta y\right] = \frac{f_0}{H_1}w_e \tag{B1}$$

$$\frac{f_0(p_1-p_2)_t}{g'H_1} - \frac{f_0(p_2-p_3)}{g'H_2} + \frac{1}{f_o}J\left[p_2, \frac{f_0(p_1-p_2)}{g'H_2} - \frac{f_0(p_2-p_3)}{g'H_2} + \beta y\right] = 0 \tag{B2}$$

$$\frac{f_0(p_2-p_3)_t}{g'H_3} - \frac{f_0(p_3-p_4)_t}{g'H_3} + \frac{1}{f_0}J\left[p_3, \frac{f_0(p_2-p_3)}{g'H_3} - \frac{f_0(p_3-p_4)}{g'H_3} + \beta y\right] = 0 \tag{B3}$$

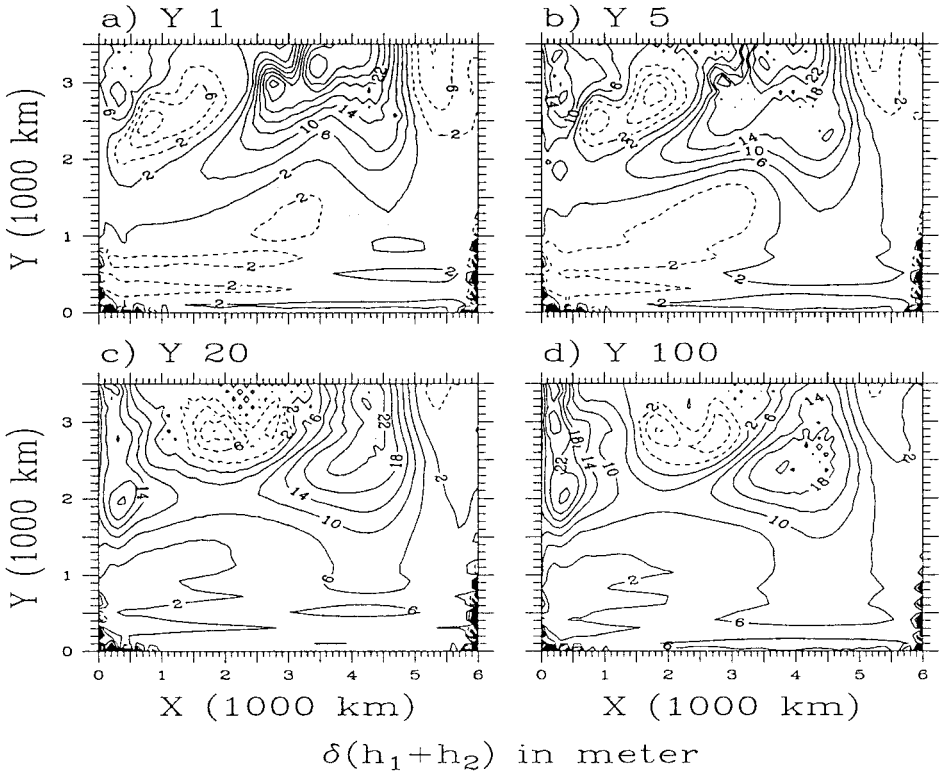

FIG. 15. Depth anomaly of the interface between the second and third layers after the enhancement of Ekman pumping, obtained from a 60 × 60 model (grid size is 100 km).

$$\frac{f_0(p_3-p_4)_t}{g'H_4}+\frac{1}{f_0}J\left[p_4,\frac{f_0(p_3-p_4)}{g'H_4}+\beta y\right]=0. \quad \text{(B4)}$$

We will assume that

$$H_1=H_2=H_3=H, \quad \text{and} \quad \epsilon=H/H_4\ll 1. \quad \text{(B5)}$$

Introducing the scalings

$$R_d^2=\frac{g'H}{f_o^2} \quad \text{(B6)}$$

$$(p_1',p_2',p_3',p_4')=\frac{1}{\beta f_o R_d^3}(p_1,p_2,p_3,p_4) \quad \text{(B7)}$$

$$t'=\beta R_d t \quad \text{(B8)}$$

$$w'=\frac{f_o}{\beta^2 R_d^2 H}w, \quad \text{(B9)}$$

and dropping the primes, yields

$$(p_2-p_1)_t+J[p_1,p_2-p_1+\beta y]=w \quad \text{(B10)}$$

$$(p_1-p_2)_t-(p_2-p_3)_t+J[p_2,p_1-2p_2+p_3+\beta y]=0 \quad \text{(B11)}$$

$$(p_2-p_3)_t-(p_3-p_4)_t+J[p_3,p_2-2p_3+p_4+\beta y]=0 \quad \text{(B12)}$$

$$\epsilon(p_3-p_4)_t+J[p_4,\epsilon(p_3-p_4)+\beta y]=0, \quad \text{(B13)}$$

where the nondimensional $\beta=\beta_{\text{dimensional}}R_d/f_o$.

We now separate the variables into steady and time-dependent parts, for example,

$$p_i=P_i+p_i,\ i=1,2,3,4. \quad \text{(B14)}$$

In addition, we introduce

$$p_1-p_2=h_1, \qquad p_2-p_3=h_2,$$
$$p_3-p_4=h_3. \quad \text{(B15)}$$

Thus

$$-h_{1t}+J[P_1,-h_1]+J[p_1,P_2-P_1+\beta y]=w \quad \text{(B16)}$$

$$h_{1t}-h_{2t}+J[P_2,h_1-h_2]+J[p_2,P_1-2P_2+P_3+\beta y]=0 \quad \text{(B17)}$$

$$h_{2t}-h_{3t}+J[P_3,h_2-h_3]+J[p_3,P_2-2P_3+P_4+\beta y]=0 \quad \text{(B18)}$$

$$\epsilon h_{3t}+J[P_4,\epsilon h_3]+J[p_4,\epsilon(P_3-P_4)+\beta y]=0. \quad \text{(B19)}$$

Dividing the last equation by ϵ and summing up these four equations yields the Sverdrup relation

$$J\left[p_1 + p_2 + p_3 + \frac{1}{\epsilon}p_4,\ \beta y\right] = w \tag{B20}$$

$$p_1 + p_2 + p_3 + \frac{1}{\epsilon}p_4 = \frac{w}{\beta}(x - x_e). \tag{B21}$$

a. Deep lowest-layer approximation

In many applications, the lowest layer is much thicker than the shallower layers. Thus, the ϵ terms in (B21) can be neglected, and the pressure in the lowest layer is constant. This assumption greatly simplifies the equations

$$-h_{1t} - J[P_1, h_1] - J[P_2 - P_1 + \beta y,\ h_1 + h_2 + h_3] = w \tag{B22}$$

$$h_{1t} - h_{2t} + J[P_2, h_1 - h_2] - J[P_1 - 2P_2 + P_3 + \beta y, h_2 + h_3] = 0 \tag{B23}$$

$$h_{2t} - h_{3t} + J[P_3,\ h_2 - h_3] - J[P_2 - 2P_3 + \beta y,\ h_3] = 0. \tag{B24}$$

b. The characteristics approach

The general case with a mean flow is difficult; in fact, there is no complete theory about hyperbolic systems with three or more variables. Thus, we begin with the case of no mean flow, and the basic equations reduce to

$$-h_{1t} + \beta(h_1 + h_2 + h_3)_x = w \tag{B25}$$

$$(h_1 - h_2)_t + \beta(h_2 + h_3)_x = 0 \tag{B26}$$

$$(h_2 - h_3)_t + \beta h_{3x} = 0. \tag{B27}$$

Following classical characteristics theory, a linear combination of these equations is formed, that is, (B25) + λ_* (B26) + γ_* (B27)

$$[(\lambda - 1)h_1 + (-\lambda + \gamma)h_2 - \gamma h_3]_t + \beta[h_1 + (1 + \lambda)h_2 + (1 + \lambda + \gamma)h_3]_x = w. \tag{B28}$$

The condition for a general coordinate to be a characteristic is that the differentiation of time and space should occur as an implicit differentiation, thus

$$\frac{\lambda - 1}{1} = \frac{-\lambda + \gamma}{1 + \lambda} = \frac{-\gamma}{1 + \lambda + \gamma}.$$

This leads to a cubic equation for λ

$$\lambda^3 + 2\lambda^2 - \lambda - 1 = 0,$$

with roots

$$\lambda_i = 0.801938, \quad -0.554958, \quad -2.245980;$$

hence,

$$\gamma_i = 0.445042, \quad -1.246980, \quad 1.801938.$$

If the mean flow is nontrivial, the linearly combined equation is

$$[(\lambda_i - 1)h_1 + (\gamma_i - \lambda_i)h_2 - \gamma_i h_3]_t - J[P_1, h_1] - J[P_2 - P_1 + \beta y, h_1 + h_2 + h_3] + J[\lambda_i P_2, h_1 - h_2] - J[\lambda_i(P_1 - 2P_2 + P_3 + \beta y), h_2 + h_3] + J[\gamma_i P_3, h_2 - h_3] - J[\gamma_i(P_2 - P_3 + \beta y), h_3] = w.$$

Since there are linear relations between the new functions we write

$$M_i = a_{1i}h_1 + a_{2i}h_2 + a_{3i}h_3, \qquad \text{or } M = \mathbf{A}h,$$

where

$$\mathbf{A} = \begin{pmatrix} -0.198062 & -0.356896 & -0.445042 \\ -1.554958 & -0.692021 & 1.246980 \\ -3.246980 & 4.048917 & -1.801938 \end{pmatrix}.$$

Inverting matrix $\mathbf{A}$, one has

$$h = \mathbf{B}M,$$

where

$$\mathbf{B} = \mathbf{A}^{-1} = \begin{pmatrix} -0.543134 & -0.349292 & -0.107574 \\ -0.978694 & -0.155449 & 0.134143 \\ -1.220411 & 0.280110 & -0.059699 \end{pmatrix}.$$

Thus, we have the three characteristic equations

$$M_{it} + \sum_{j=1}^{3} J[-b_{1j}P_1 + \lambda_i(b_{1j} - b_{2j})P_2 + \gamma_i(b_{2j} - b_{3j})P_3 - (b_{1j} + b_{2j} + b_{3j})(P_2 - P_1 + \beta y) - \lambda_i(b_{2j} + b_{3j})(P_1 - 2P_2 + P_3 + \beta y) - \gamma_i b_{3j}(P_2 - 2P_3 + \beta y),\ M_j] = w.$$

This can be rewritten as

$$M_{it} + J[\chi_{i1}, M_1] + J[\chi_{i2}, M_2] + J[\chi_{i3}, M_3] = w.$$

We now have identified the three dependent variables M_1, M_2, M_3, and for each of them, we have a characteristic equation; namely,

$$M_{it} + J[\chi_{ii}, M_i] = w - \sum_{i \neq j} J[\chi_{ij}, M_j],$$

where $\boldsymbol{\chi} = [\chi_1, \chi_2, \chi_3]^{\mathrm{T}} = [\chi_{ii}]^{\mathrm{T}}$ defines the characteristics,

$$\chi = \mathbf{C}P \qquad \mathbf{C} = \begin{pmatrix} 0.543134 & 0.349292 & 0.107574 & 2.742238 & 1.763545 & 0.543134 \\ 0.349292 & 0.107574 & 0.543134 & 0.224631 & 0.069182 & 0.349292 \\ 0.107574 & 0.543134 & 0.349292 & 0.033131 & 0.167274 & 0.107574 \end{pmatrix}$$

$$\mathbf{P} = \begin{pmatrix} P_1 \\ P_2 \\ P_3 \\ P_2 - P_1 + \beta y \\ P_1 - 2P_2 + P_3 + \beta y \\ P_2 - 2P_3 + \beta y \end{pmatrix}.$$

REFERENCES

Deser, C., M. Alexander, and M. Timlin, 1996: Upper-ocean thermal variability in the North Pacific during 1970–1991. *J. Climate*, **9,** 1840–1855.

Dewar, W. K., 1986: On the potential vorticity structure of weakly ventilated isopycnals: theory of subtropical mode water maintenance. *J. Phys. Oceanogr.*, **16,** 1204–1216.

——, 1998: On ''too fast'' baroclinic planetary waves in the general circulation. *J. Phys. Oceanogr.*, **28,** 1739–1758.

Henderschott, M., 1989: The ventilated thermocline in quasigeostrophic approximation. *J. Mar. Res.*, **47,** 33–53.

Huang, R. X., 1989: Sensitivity of a multilayered oceanic general circulation model to the sea surface thermal boundary condition. *J. Geophys. Res.*, **94,** 18 011–18 022.

——, 2000: Climate variability inferred from the continuously stratified model of the ideal-fluid thermocline. *J. Phys. Oceanogr.*, **30,** 1389–1406.

——, and K. Bryan, 1987: A multilayer model of the thermohaline and wind-driven ocean circulation. *J. Phys. Oceanogr.*, **17,** 1909–1924.

——, and S. Russell, 1994: Ventilation of the subtropical North Pacific. *J. Phys. Oceanogr.*, **24,** 2589–2605.

——, and B. Qiu, 1998: The structure of the wind-driven circulation in the subtropical South Pacific Ocean. *J. Phys. Oceanogr.*, **28,** 1173–1186.

——, and J. Pedlosky, 1999: Climate variability inferred from a layered model of the ventilated thermocline. *J. Phys. Oceanogr.*, **29,** 779–790.

——, and ——, 2000: Climate variability induced by anomalous buoyancy forcing in a multilayer model of the ventilated thermocline. *J. Phys. Oceanogr.*, **30,** 3009–3021.

Joyce, T., C. Deser, and M. Spall, 2000: The relation between decadal variability of Subtropical Mode Water and the North Atlantic Oscillation. *J. Climate*, **13,** 2550–2569.

Killworth, P. D., D. Chelton, and R. de Szoeke, 1997: The speed of observed and theoretical long extratropical planetary waves. *J. Phys. Oceanogr.*, **27,** 941–962.

Levitus, S., 1989: Interpentadal variability of temperature and salinity at intermediate depths of the North Atlantic Ocean, 1970–1974 versus 1955–1959. *J. Geophys. Res.*, **94** (C5), 6091–6131.

Liu, Z., 1999: Forced planetary wave response in a thermocline gyre. *J. Phys. Oceanogr.*, **29,** 1036–1055.

Luyten, J., J. Pedlosky, and H. Stommel, 1983: The ventilated thermocline. *J. Phys. Oceanogr.*, **13,** 292–309.

Marshall, J., G. Nurser, and R. Williams, 1993: Inferring the subduction rate and period over the North Atlantic. *J. Phys. Oceanogr.*, **23,** 1315–1329.

Pedlosky, J., and W. R. Young, 1983: Ventilation, potential vorticity homogenization and the structure of the ocean circulation. *J. Phys. Oceanogr.*, **13,** 2020–2037.

Qiu, B., and R. X. Huang, 1995: Ventilation of the North Atlantic and North Pacific: Subduction versus obduction. *J. Phys. Oceanogr.*, **25,** 2374–2390.

——, W. Miao, and P. Mueller, 1997: Propagation and decay of forced and free baroclinic Rossby waves in off-equatorial oceans. *J. Phys. Oceanogr.*, **27,** 2405–2417.

Rhines, P., and W. Young, 1982: A theory of the wind-driven circulation. I. Mid-ocean gyres. *J. Mar. Res.*, **40** (Suppl.), 559–596.

White, W., Y. Chao, and C.-K. Tai, 1998: Coupling of biennial oceanic Rossby waves with the overlying atmosphere in the Pacific basin. *J. Phys. Oceanogr.*, **28,** 1236–1251.